SLAC–PUB–6723
SLAC/SSRL–0097
November 1994
(SSRL–M)

PHASE SEPARATION IN SPUTTERED AMORPHOUS METAL-GERMANIUM ALLOYS

Michael J. Regan* and Arthur Bienenstock
Stanford Synchrotron Radiation Laboratory, Stanford Linear Accelerator Center
M.S. 69, P.O. Box 4349, Stanford CA, 94309

PACS 61.43.Dq, 61.10.Lx, 68.55.-a, 71.30.+h

ABSTRACT

Anomalous small-angle x-ray scattering (ASAXS) has been used to observe and characterize phase separation in sputtered amorphous Fe_cGe_{1-c} and Mo_cGe_{1-c} thin films. Significant chemical inhomogeneity and anisotropy is observed. At low metal concentrations ($c<0.25$), no films are homogeneous nor isotropic through the metal-insulator transition composition region ($10\leq c\leq 25$). Measurements performed with the scattering vector both in and oblique to the film surface plane indicate that the chemical inhomogeneities are quite anisotropic. The cylindrical correlation functions, which have been calculated from the oblique scattering with a spherical harmonics approach, suggest a physical picture in which well-correlated inhomogeneities are formed at the surface during film growth, with little correlation between those formed in one layer and those formed after 2 nm of material have been deposited. These results suggest that fluctuations in the growth direction play a pivotal role in preventing simple columnar structure growth or structures that evolve systematically as the film grows. In addition, the anomalous scattering measurements confirm that the metal atoms (Fe or Mo) are the source of the inhomogeneity, with the Ge atoms distributed homogeneously. A method for using these measurements to determine the compositions of the phase-separating species has been developed. The results indicate phase separation into endpoint compositions of amorphous Ge and an intermetallic phase of composition close to $FeGe_2$ or $MoGe_3$. Finally, by manipulating the deposited power flux and rates of growth, Fe_cGe_{1-c} films which have the same Fe composition can be grown to different states of phase separation. These results may help explain the difficulty workers have had in isolating the metal-insulator transition for these and other vapor-deposited amorphous alloys.

I. INTRODUCTION

Amorphous metal-germanium vapor-deposited films have been studied extensively over the past 15 years. Much of the effort has been aimed at understanding the metal-insulator (M-I) transitions in the region of 10-25 at. % metal. Superconducting transitions in the Mo-Ge system and magnetic transitions in the Fe-Ge system have also attracted considerable attention. These two systems have been of particular interest because they remain amorphous through the transitions.

Work supported in part by Department of Energy Contract DE-AC03-76SF00515.

Submitted to *Physical Review B: Condensed Matter*

Almost all attempts to interpret the measured physical properties of the Mo-Ge and Fe-Ge systems have assumed, implicitly, that the films are chemically homogeneous. In recent years, however, it has become increasingly clear that at least some of the films are not homogeneous--and that the inhomogeneities have a significant influence on the physical properties.

Initial evidence of phase separation in sputtered amorphous Mo_cGe_{1-c} films came from Kortright and Bienenstock,[1] who studied them with EXAFS, differential anomalous scattering (DAS) and small-angle x-ray scattering (SAXS). They provided strong, but not conclusive, evidence for the coexistence of tetrahedral a-Ge with a very fine scale (<4 nm) Mo-modified amorphous material in the composition region $0 \leq c < 0.23$. Their work indicates that the local order in the modified material resembles that of the crystalline Ge-rich compounds (e.g., $MoGe_2$ or $Mo_{13}Ge_{23}$, the only Ge-rich compounds in the equilibrium phase diagram). At approximately c=0.23, no evidence of the tetrahedral a-Ge or chemical inhomogeneities remains. The structures in the region $0.23 \leq c \leq 0.50$ are typical of most intermetallic structures (long Mo-Mo distances, strong ordering of Ge around Mo). The collapse of the long Mo-Mo distances leads to a third region, c>0.5, in which the structure is similar to that found in most melt-quenched metal-metalloid glasses. These authors were unwilling to state definitively that the material is phase-separated in the M-I transition region $0 \leq c < 0.23$ because the SAXS they observed might have arisen from voids or other defects.

The electrical transport properties shed little light on the question of homogeneity. Yoshizumi et al.[2] found the M-I transition at c=0.10 for sputtered amorphous Mo_cGe_{1-c} alloys and superconducting transitions at Mo concentrations as low as c=0.135. For co-evaporated samples, Devenyi et al.[3] conclude that the M-I transition occurs between c=0.075 and 0.16, for which they had prepared samples.

Specific heat measurements on co-sputtered amorphous Mo-Ge alloys by Mael et al.[4] indicate that there exists no critical behavior of the thermodynamic electronic density of states, proportional to the linear term in the specific heat, at the M-I transition. They show that a non-vanishing density of states exists on the insulating side of the M-I transition and is considerably larger than that of pure a-Ge. They associate these states with the Mo-modified material proposed by Kortright and Bienenstock.[1]

Similarly, the atomic scale structure of triode-sputtered Fe_cGe_{1-c} alloys has been studied as a function of composition by Lorentz et al.[5] with SAXS and x-ray absorption near edge structure (XANES). For c>0.33, these authors found phase separation through the magnetic-nonmagnetic transition, which suggests the transition occurs through a percolation of a-Fe_3Ge within a-$FeGe_2$. As in the x-ray study of Mo-Ge cited above, however, their methods were not sensitive to composition modulations on a fine size scale (<4 nm), so they could not rule out separation for c<0.33.

For co-evaporated amorphous Fe_cGe_{1-c} films, Daver et al.[6] cite a M-I transition composition as c=0.25 on the basis of resistivity measurements. In contrast, the M-I transition for the triode-sputtered Fe-Ge films studied by Lorentz et al. is cited as occurring at 15 at.% Fe. While these M-I transition compositions can be interpreted in terms of either homogeneous or inhomogeneous materials, the difference in compositions for co-evaporated and triode sputtered Fe_cGe_{1-c} materials suggests a microstructural difference.

Ding and Andersen[7] performed molecular-dynamics computer simulations on the structure of amorphous Mo-Ge and noticed that Mo at low concentrations does not substitute for Ge but rather tends to cluster, forming chains and rings, and hence distorts the local Ge random tetrahedral network, as predicted. This supports Kortright and Bienenstock's model of a Mo-modified

material, but since the amorphous state in their simulation was formed by rapidly cooling a theoretical "melt" of Mo and Ge atoms, the simulation cannot explain structural effects that depend on the kinetics of the vapor deposition process itself. In the work reported here, we have found that both the direction of film growth and deposition parameters are essential to specifying the degree and extent of phase separation.

TEM studies[8] (Mo-Ge alloys) have had similar difficulties in detecting such a fine scale separation for $c<0.25$. Electron microscopy has been used to observe composition modulations in the amorphous Au-Si system[9], which shows considerably greater contrast. As will be shown in this paper, however, with anomalous small-angle x-ray scattering[10] (ASAXS), variable electron density contrast and statistical averaging of fine scale modulations, among other features, become possible.

The existence of composition fluctuations on an extremely fine scale was shown definitively by Rice et al.[11] who used ASAXS to distinguish chemical fluctuations on a 15-30 Å scale from voids, cracks and similar defects in amorphous Fe_cGe_{1-c}, Mo_cGe_{1-c} and W_cGe_{1-c} sputtered films.

Some of the conclusions of this work have been presented in a recent paper.[12] In this work, the characterization of the composition fluctuations in magnetron sputtered amorphous Fe_cGe_{1c} and Mo_cGe_{1-c} films, which led to some of those conclusions, is described in more detail. It is shown that the following has been determined:

1) The metal-rich "particle" sizes are anisotropic, with diameters of the order of 1 nm in the growth plane and 1.5-2.0 nm in the growth direction. These sizes indicate that a columnar description is inappropriate.

2) The interparticle correlations are also anisotropic. A well-defined depletion region surrounds the particles in the growth plane, whereas the depletion region is non-existent or extremely small in the growth direction.

3) If it is assumed that one phase is a-Ge, then the others have compositions close to $FeGe_2$ and $MoGe_3$ in the M-I transition regions of the Fe-Ge and Mo-Ge films, respectively.

4) The phase separation microstructure can be manipulated by altering the deposition conditions.

5) Fluctuations (probably associated with variations in adatom flux or sputtered metal clusters) disrupt the growth process to prevent the formation of long columns. That is, there is copious nucleation if the system separates by nucleation and growth. If the process is closer to spinodal decomposition, then fluctuations frequently interrupt the decomposition process.

6) This extremely fine scale, anisotropic phase separation can be characterized by ASAXS, particularly through the use of cylindrical correlation functions introduced by Norman[13] and the oblique transmission SAXS approach introduced by Cargill.[14]

We begin in Section II with a discussion of sample preparation, x-ray absorption methods, and the ASAXS technique. Section III is devoted to the k-space scattering results, while Section IV discusses our methods to isolate the endpoint compositions. Finally, Sections V and VI focus on the real-space interpretation of our results, first in terms of correlation functions and then in terms of specific models of a simplified, anisotropic phase separation.

II. EXPERIMENTAL AND SAMPLE CHARACTERIZATION

A. Sample Preparation

Amorphous Fe_cGe_{1-c} (c = 0.058, 0.062, 0.063, 0.087, 0.107, 0.108, 0.115, 0.136, 0.182, 0.239, 0.251, 0.270, 0.439 and 0.466) and Mo_cGe_{1-c} (c = 0.065, 0.124, 0.165 and 0.236) alloys were prepared at room temperature by magnetron co-sputtering of elemental targets onto a rapidly rotating substrate table, so that only a fraction of a monolayer is deposited as the sample is rotated in front of one target and then the next. The sputtering geometry was in the vertical, with the substrate table always positioned 3" below the planar magnetron sputter guns. The base pressure of the chamber was never higher than $2x10^{-6}$ Torr, and the sputtering gas, purified Ar, always held at 2 mTorr.

The Ge RF power was usually set in the range of 350-400 watts (except for some samples grown at ~100 watts to determine the effect of varying target power on the degree of phase separation), while the Mo or Fe DC current was varied from 0.02-0.20 amperes to control the overall composition of the film (for c<0.33). The substrates consisted of clean Si (100) wafers, glass microscope slides, and 25 μm Kapton. Film growth rates varied from 1-4 Å/sec depending on target power settings, but typically 5-10 μm thick films could be grown in 7-10 hours. With a table rotation of 300 rpm, approximately 0.2 to 0.8 Å of material are deposited for each revolution under the sputter guns. The films were grown to such thicknesses that they could support their own weight and not crack or flake once the Si support was removed. For films thicker than 6-7 μm, the Si substrates could be rendered free-standing by etching the Si substrates in a KOH bath. All the ASAXS spectra presented in this work are from free-standing samples, except for those presented in fig. 3.

After sputtering, the films were smooth with a shiny surface. A conventional Picker x-ray diffractometer was used to ensure that the samples used in this study had not crystallized. Since there was no etch stop protecting the films, there was concern that the Si substrate removal procedure with KOH may have damaged the films. There was no visual evidence for such damage, however, and the diffractometer scans showed no change between the free-standing films and those that were Kapton-supported. These observations are in agreement with Wilson,[15] who also observed no change in large-angle scattering of Mo-Ge alloys with KOH etch. Additionally, the ASAXS patterns show no difference between the free-standing and Kapton-supported films (from the same deposition), except for the far-improved signal-to-noise ratio (SNR) from the free-standing film. An alpha-step profilometer was used to determine the film thickness and an electron microprobe to determine the atomic percent metal in each alloy.

B. X-ray Absorption Measurements

X-ray absorption measurements were performed near the relevant atomic absorption edge energies to determine the anomalous scattering factors for use in differential anomalous scattering (DAS),[16] as well as to provide additional information about the film thicknesses and compositions. The data were acquired on the eight-pole wiggler side-stations 4-1 and 4-3 of the Stanford Synchrotron Radiation Laboratory (SSRL) for all of the sputtered films, which were at room temperature. For the Fe-Ge alloys, Si(111) crystals were used to scan the Ge K-edge (11103 eV) over the energy range of 10858 eV to 12070 eV and the Fe K-edge (7102 eV) from 6866 eV to 8078 eV. For the Mo-Ge alloys, Si(220) crystals were used. The relevant scan ranges were 10858 eV to 12071 eV for the Ge K-edge and 19555 eV to 21226 eV for the Mo K-edge (20000 eV).

f′(E) and f″(E), the real and imaginary parts, respectively, of the anomalous components of the atomic scattering factor were obtained from the x-ray absorption data with standard procedures.[17] The absorption measurements were also used to determine the films' compositions, using the method of Wilson.[15] Since this method measures the composition of the entire thickness of the sample, whereas the electron microprobe only samples the top ~1000 Å, we have used the atomic fractions determined from the x-ray approach. Compositions determined by the two methods did not differ by more than 5-10%, which translates to less than 1-2 at.% metal for the concentrations studied. This also indicates that there is little change in metal concentration with film thickness. By assuming an average number density for the overall film, n_{avg}, the thickness can be calculated. For a given film of metal concentration c (c<0.33), n_{avg} was taken as 95% of the weighted average number densities of crystalline Ge, $MoGe_2$, and $FeGe_2$. Results are consistent with the alpha-step profilometer.

C. ASAXS Method

The ASAXS camera used for the measurements, SSRL beam line x-ray optics, energy resolution, and data manipulation have been described in detail elsewhere.[18,19] Data were collected at the eight-pole wiggler end-station 4-2 at SSRL. Depending on the x-ray energy, either Si(111) or Si(220) monochromator crystals were used in a double-crystal configuration. Besides an upstream aperture to limit the vertical and horizontal beam divergence, the incident beam was further defined in the hutch by two sets of slits (each approximately 0.25 mm vertical by 0.50 mm horizontal) separated by an evacuated chamber which could be varied from one to three meters in length. The samples were held in transmission and separated by a telescoping, evacuated chamber from a linear position-sensitive detector. Miniature ionization chambers, placed directly before and after the sample, were used to normalize scattering data as well as to calibrate the monochromator. The monochromator, ion chambers, and detector were all controlled by a micro-VAX through a CAMAC interface.

Depending on the x-ray energy, the windows used to separate the evacuated chambers and air were either 25 μm mica or Kapton. Mica is the preferred material, except that it contains enough Fe to prohibit its use for DAS studies at the Fe edge. Consequently, mica has been used at the Mo and Ge edges, and Kapton at the Fe edge (and occasionally at the Ge edge, as well). Unfortunately, Kapton has appreciable small-angle scattering in the angular region of interest, and, even with the free-standing films, the Kapton scattering from the windows on the evacuated chambers is noticeable and must be subtracted. Especially at the Mo edge, where the reduced counting efficiency limits the SNR, elimination of all Kapton with mica led to significant changes in the scattering pattern with energy which were somewhat obscured during a previous attempt.

Experiments were performed on all samples with the x-ray beam at normal incidence to the films. For the Fe_cGe_{1-c} samples with c = 0.063, 0.108, 0.136 and 0.182, as well as the Mo_cGe_{1-c} samples with c = 0.065 and 0.124, oblique incidence was also utilized by tilting the sample through an angle θ_k (see fig. 1). A broad range of orientations of the scattering vector with respect to the sample plane are available. To achieve this, a Huber 410 circle, which was affixed to the camera's optical rail, provided the necessary sample rotation. The data sets consist of radial scans in $\vec{k}$-space; that is, the sample was taken to a particular tilt angle θ_k, so that in the small-angle limit the direction of $\vec{k}$ was fixed, and the scattering was measured as a function of the scattering vector magnitude k. This was done for θ_k=90, 75, 60, 45, 30, and 15° (0° is not measurable) and 4-6 x-ray energies per absorption edge.

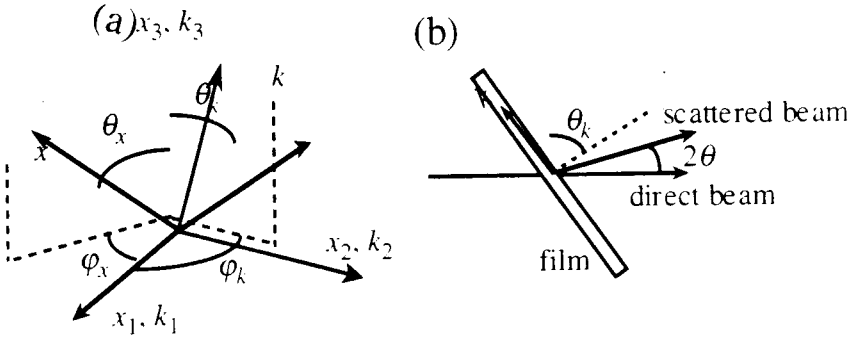

Fig. 1. (a) Real and reciprocal space coordinate systems. (b) X-ray scattering geometry. $|\vec{k}| = 4\pi\sin(2\theta/2)/\lambda$, with 2θ the scattering angle and λ the x-ray wavelength.

There was essentially no dark current with the beam off (1-5 cps integrated along the length of the detector), so that it was ignored. The observed scattering was then a combination of the coherent and incoherent processes in the sample and that from window materials, air, etc. ('background"). The range of reciprocal space covered depends on the sample-detector distance and the incident x-ray energy, but typical values ranged from k=0.005 to 0.60 $Å^{-1}$. Smearing effects due to finite beam size have been considered. They are, however, negligible due to the small spot size used and relatively large small-angles studied and, hence, are ignored in the analysis.

The position sensitive detector used in the measurements was a 20 cm linear position sensitive proportional counter with a 6 mm conversion depth. The counter gas was typically a 70% Ar/balance CO_2 mixture which has a 1/e absorption length of 4.0 cm at 7 keV (Fe edge at 7112 eV). In order to record the Mo edge (20000 eV) coherent scattering and perform DAS, however, an 80% Xe/balance CO_2 counter gas that gave an absorption length of 8.2 cm at the Mo edge was used. (The absorption length is too large, 77 cm at these hard x-rays, for the Ar-containing gas.) This was still not sufficient, however, to carry out DAS since the large fraction of Ge in the samples swamped the detector with fluorescence ($K\alpha_1$=9886, $K\alpha_2$=9855, $K\beta_1$=10982, $K\beta_3$=10975 eV). These lower energy photons are distributed over 4π solid angle and are detected as a constant background superimposed on the coherent scattering. With the fluorescence emitted at lower energies and, hence, preferentially absorbed in the limited detector depth (absorption length is 1.5 cm for the Xe mixture at 10 keV), the count rates are so large that space-charge effects and dead time corrections become appreciable. Although the detector energy resolution is approximately 20% and the fluorescence can be discriminated, the beam flux must be reduced in any case to avoid the high count rates, and the resulting SNR is not good enough to perform DAS.

To avoid this problem, a large, sputtered Zn filter [which has an absorption edge between the fluorescent radiation and the coherent signal (Zn K-edge at ~9.7 keV)] was placed over the linear detector, downstream of the beamstop, so the Ge fluorescence could be preferentially absorbed without excitation of Zn fluorescence from the direct beam. The Zn filter, sputtered from a Zn target onto a large sheet of 25 μm Kapton, was ~4.8 μm thick. Two filters, stacked one on top of the other for a net ~9.6 μm Zn, worked best.

For measurements at the Ge edge, we have used both Ar- and Xe-containing gases, but all data presented here at these energies are from collection with the Xe-containing gas. Fluorescence from Fe at x-ray energies near the Ge edge in the Fe-Ge samples was not so great as to warrant the use of an absorbing filter and was removed with the background subtraction method outlined next.

This is due to the small Fe concentrations studied and the low fluorescence yield of the lighter elements.

The spectra were: (a) corrected for background scattering which is present in the absence of a sample, (b) normalized to incident intensity, sample absorption and thickness, and (c) placed on an absolute scale with polyethylene.[20] There remained, however, the issue of isolating the sample's coherent scattering, the differential cross-section per sample volume $d\sigma/d\Omega$, which is superimposed on the angular-independent incoherent scattering, $\Re$, given as $d\sigma(\vec{k},E)/d\Omega + \Re(E)$.

The background in these data were subtracted in the following way (similar to that by Maret et al.[21]). For a particular sample and oblique transmission angle, the coherent scattering at sufficiently large k was assumed to follow a power law of the form

$$\frac{d\sigma(k,\theta_k,E)}{d\Omega} + \Re(E) = A(E,\theta_k)/k^{\alpha} + B(E,\theta_k). \qquad (1)$$

The B was then removed from each scan, rendering $d\sigma(k,\theta_k,E)/d\Omega$. Initially, we tried to determine A, α and B in Eq. 1 using a non-linear least-squares routine to fit the observed scattering. The results were inconclusive, however, since the relevant k range that can be fit is less than a decade--limited by the large interparticle interference at small k and the poor SNR at larger k and is extremely sensitive to errors.

Subsequently, more directed possibilities were examined. For the case of a broad SAXS maximum from amorphous Tb-Cu and Gd-Cu alloys, Maret et al.[21] used the Porod scattering power-law for sharp interfaces, α=4, to fit their data. Schmidt et al.[22] have found that power-law scattering exponents that are fit over several decades in k may differ (~10%) from a local power-law fit over smaller ranges in k. They have shown that the SAXS at large k can decay at a rate greater than k^{-4} and as great as k^{-6}. We found it impossible to determine α uniquely over the range 4-5. Since that was the case, the coherent scattering was extracted using two different values of α, 4 and 5, to test the sensitivity of physical results to the choice of α. A more detailed analysis of the large-k scattering can be found in Ref. 19.

In this work, the partial structure factors (PSFs) are the quantities most likely to be sensitive to a poor background correction. We found, however, that they are fairly insensitive to the method of background subtraction, as long as it is performed in some consistent way. The background subtraction method is also important when calculating the total coherent cross-section and is discussed in greater detail in Section IV.

III. SCATTERING RESULTS

A. Amorphous Fe_cGe_{1-c}

Fig. 2 shows the differential cross-section per sample volume determined from the oblique transmission experiment for three Fe_cGe_{1-c} samples. A strong anisotropy is evident from the change in the scattering peak with sample orientation. As the scattering vector direction moves from sample surface to sample normal there is a sharp, monotonic decrease in scattering intensity

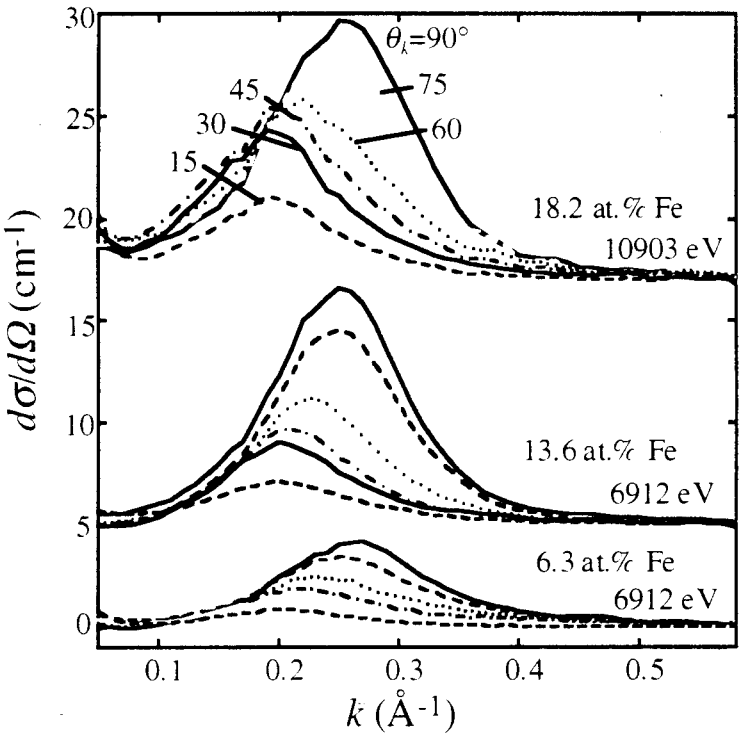

Fig. 2. Differential cross-section per unit volume for Fe_cGe_{1-c}: 18.2, 13.6, and 6.3 at.% Fe. In each case, as θ_k changes from 90 to 15°, the SAXS peak monotonically decreases in amplitude and shifts inward to smaller k. Data smoothed over an interval Δk=0.02 Å^{-1}.

and shift inward in peak position. All samples in this composition range (c<0.33) have a scattering maximum at non-zero k for $\theta_k = 90^o$. In addition, all samples for which oblique SAXS measurements were made show the general dependence on θ_k shown in fig. 2. For samples with 44 and 47 at.% Fe, however, no small-angle scattering was observed.

By changing the deposition conditions, films identical in composition can be grown to different microstructural states. Fig. 3 compares the scattering from samples of three compositions that have been prepared with two different target powers. Samples grown at 400 watts show a more "advanced" state of composition fluctuations than those at 100 watts; that is, the SAXS maximum appears at a smaller magnitude of the scattering vector with greater amplitude. The greatest change is observed for the 6 at.% Fe sample while only an intensity difference is apparent for the 25 and 27 at.% Fe samples. The change in intensity for the 25 and 27 at.% samples, however, may be due to the different overall film composition and not from the change in target power.

For all samples (<33 at.% Fe) and oblique angles studied, only slight if any changes in scattering, $d\sigma/d\Omega$, are observed as the incident photon energy is increased beneath the Ge absorption edge while there are large differences for similar changes beneath the Fe absorption edge. This observation has been made previously at normal incidence by Rice et al.[11] for amorphous Fe-Ge and W-Ge at the Fe, W, and Ge edges. These authors show that a zero variation of the intensity at the Ge edge implies that the Ge is distributed homogeneously. With our observation here of out-of-plane anisotropy in the SAXS, the range of applicability of the Rice

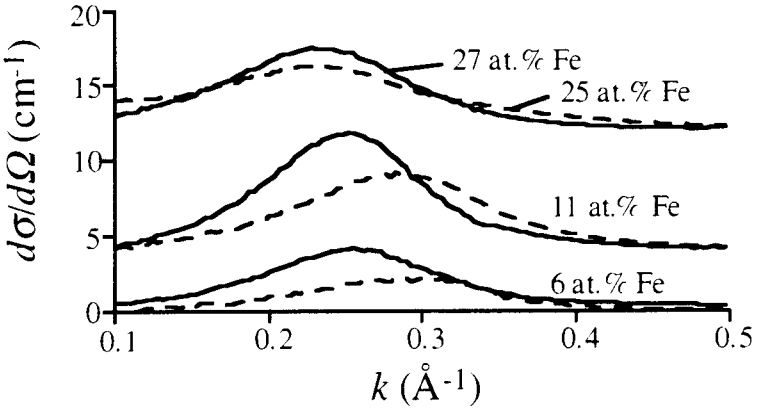

Fig. 3. $d\sigma(\vec{k},E)/d\Omega$ as a function of composition and power delivered to the sputtering targets: — 400 W power; – – – 100 W. Data smoothed over an interval Δk=0.02 Å^{-1}. Photon energy is 6912 eV.

et al. observation becomes, in principle, limited to the in-plane scattering. The measurements made here, however, indicate that the approximate Ge homogeneity holds generally.

For differences of 16% in $f_{Ge}(E)$, an approximate 4% intensity change of the main scattering peak is observed, whereas differences of 17% in $f_{Fe}(E)$ lead to a 30% intensity change. Fig. 4a shows the changes in $d\sigma/d\Omega$ at the Ge and Fe edges scaled by the relative change in $f'(E)$ for the 13.6 at.% Fe sample at normal incidence (θ_k=90°). That is, we plot

$$\frac{d\sigma(\vec{k},E_1)/d\Omega - d\sigma(\vec{k},E_2)/d\Omega}{\mathrm{abs}(f_\nu(E_1) - f_\nu(E_2))}, \tag{2}$$

for ν=Fe and Ge, E_1=-300 and E_2=-10 eV below the Ge edge, and E_1=-200 and E_2=-10 eV below the Fe edge. The large change at the Fe edge is evidence that the Fe atoms are not distributed homogeneously. A small change at the Ge edge is observed, however. Since it is approximately an order of magnitude less than the relative change at the Fe edge, our initial argument was that the Ge atoms are essentially homogeneously distributed. To verify this, the partial structure factors (PSFs) were determined.

The PSFs used here, $S_{\alpha\beta}(\vec{k})$, are defined by the equations,

$$\begin{aligned} S(\vec{k},E) = {} & c|f_{Fe}(E)|^2 S_{FeFe}(\vec{k}) \\ & + 2\sqrt{c(1-c)}\,\mathrm{Re}\left[f_{Fe}(E)\,f^*_{Ge}(E)\right] S_{FeGe}(\vec{k}), \\ & + (1-c)|f_{Ge}(E)|^2 S_{GeGe}(\vec{k}) \end{aligned} \tag{3}$$

where $S(\vec{k},E)$ is proportional to $d\sigma/d\Omega$ (scaled by the electron scattering length) and $S_{\alpha\beta}(\vec{k})$ is the Fourier transform of the α-β pair correlation function (describes the probability that a β atom is at

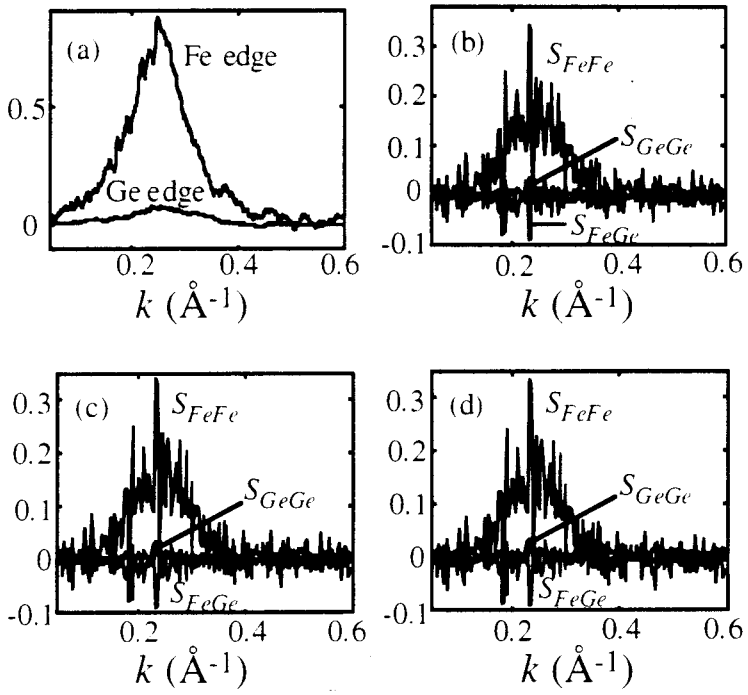

Fig. 4. (a) Absolute changes in SAXS for a 13.6 at.% Fe sample, scaled by the relative change in f ′(E), for energies 300 and 10 eV below the Ge edge and 200 and 10 eV below the Fe edge (see Eq. 2). Data smoothed over an interval $\Delta k=0.02$ Å^{-1}. (b) Normal incidence ($\theta_k=90°$) PSFs for the 13.6 at. % Fe sample determined with the Munro method (scaled by the scattering length of an electron and in units cm^{-1}). PSFs determined from scans collected at 6912, 7102, 10803, and 11093 eV. Background removed with $\alpha=4$. (c) PSFs as in (b) but with the background removed with $\alpha=5$. (d) PSFs determined as in (b) but with the background removed by assuming the coherent scattering is 0 for k>0.55 Å^{-1} for all energies and scans. Within the SNR, the PSFs appear identical and independent of the precise method of background subtraction.

$\vec{x}$ from an α atom). Since the experiment is performed at small k, the volume elements that are probed are large compared to the typical atomic volumes in the sample and, thus, the PSFs are the tranforms of the respective α-β number density correlation functions. It should be noted that the derivation of Eq. 3 assumes that there exists a center of symmetry in the pair correlation function (i.e., S_{FeGe} is real), which is always true for isotropic materials and assumed true even for this discussion of anisotropic scattering. This need not be the case, however, but the asymmetry is a subtle effect and difficult to measure in amorphous materials.[15] Extraction of the PSFs requires at least three independent data sets near atomic absorption edges where the scattering factors are changing rapidly and, hence, appreciably modifying the PSF weighting functions.

The PSFs have been extracted using the Munro[23] approach and are shown in Fig. 4 for the 13.6 at.% Fe sample in the normal transmission case ($\theta_k=90°$) and different methods of background subtraction. We have obtained similar results for the 6.3, 10.8, and 18.2 at.% Fe samples. The type of background subtraction employed seems to have little effect on the results, whether the

data are fit to power laws with α=4 or 5 or are aligned at large k~0.55 Å^{-1}. There appears little, if any, Ge contribution to the total scattering pattern.

The S_{FeGe} and S_{GeGe} are essentially zero throughout the k-range measured, indicating clearly that the conclusion based on the difference at the Ge K-edge is valid. That is, the Ge atoms are essentially homogeneously distributed. This situation holds for all oblique angles and compositions studied (c<0.33). $S(\bar{k},E)$ appears comprised solely of S_{FeFe}, which must also be responsible for the anisotropy or change in correlation with film orientation. This result also implies that, for all samples, voids do not contribute appreciably to the SAXS over this k-range, since they would be observed as a non-zero S_{GeGe}.

One aspect of these PSFs is troublesome. Fig. 4a shows a clear, but small difference at the Ge edge, but there is no observable manifestation of it in the PSFs. One might dismiss this as a consequence of poor SNR and large condition numbers in the linear equations relating the PSFs to the measured intensities. The fact that the Ge-Ge and Fe-Ge partials seem to oscillate directly around zero with relatively small amplitudes leaves one uneasy about that conclusion. From the Ge difference signal in fig. 4a, it does not appear as if the SNR and the condition numbers are sufficiently bad to prevent us from properly inverting Eq. 3 to solve for the PSFs. This is particularly disconcerting since the S_{GeGe} should have the greatest accuracy of the three partials because of the high Ge concentration in this sample and because $f_{Ge}>f_{Fe}$. We do not understand this insensitivity of the analysis to the small, but measurable, Ge difference.

B. Amorphous Mo_cGe_{1-c}

Fig. 5 illustrates the structure factor at normal incidence for several Mo_cGe_{1-c} (0.065<c<0.236) alloys collected at an x-ray energy of 10803eV with a Xe/CO_2 gas filled detector. The scattering is much weaker than that recorded from the Fe-Ge alloys. The backgrounds have

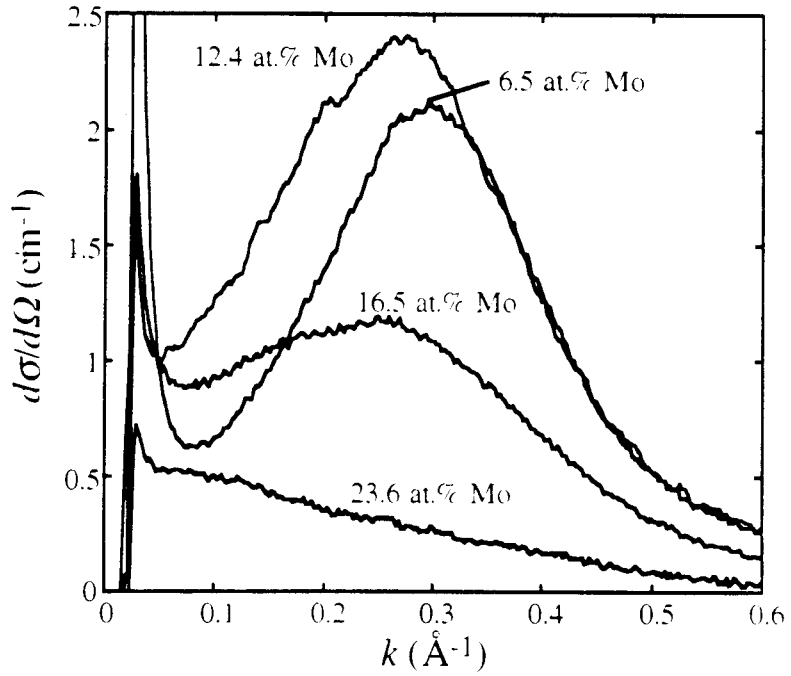

Fig. 5. $d\sigma(\bar{k},E)/d\Omega$ at normal incidence as a function of composition for several Mo_cGe_{1-c} alloys. Photon energy is 10803 eV.

been subtracted and the data put on an absolute scale. The 6.5 and 12.4 at.% Mo samples exhibit the greatest magnitude of scattering, with it less intense for the 16.5 at.% Mo sample, while little scattering is recorded for 23.6 at.% Mo.

The scattering that is recorded for 23.6 at.% Mo is extremely weak and is of a different kind, at small k, with only a small scattering maximum resolvable. Kortright and Bienenstock[1] did not observe appreciable SAXS of any kind for their 25 at.% Mo sample (grown under identical conditions as the 23.6 at.% Mo sample reported here) in the small-angle region spanning $0.01<k<0.15$ Å^{-1} so it is possible that the apparent maximum near $k\sim0.1$ Å^{-1} may result from an imperfect subtraction of the mica windows and/or from parasitic scattering from and around the main beam. This is unlikely, however, since we have observed this sample's scattering pattern during different data collection periods as well as during a single collection period but with different camera lengths. It is thus likely that the small SAXS reported for this sample indicates that the volume fraction of the chemical inhomogeneity is decreasing rapidly and becomes essentially zero at ~25 at.% Mo. Attempts with DAS to verify that this is, in fact, the case, have not been successful. Differences in the extremely small SAXS signal at energies near the Ge and Mo edges lead to such poor SNRs that prevent a systematic study at this composition with DAS.

The oblique transmission results for the 6.5 at.% Mo sample recorded at 7100 eV are presented in Fig. 6a. The anisotropy is not strong, as the intensity of the $\theta_k=90°$ scan is only slightly stronger than that of the 60° scan. The anisotropy in the Fe_cGe_{1-c} samples is far more pronounced, with the $\theta_k=90°$ scan ~5 times that of the 60° scan, but the fractional changes in the positions of the SAXS maxima with θ_k appear similar for the Fe- and the Mo-containing alloys. The positions of the maxima are, of course, dependent on the concentration of the metal atoms, but, for similar compositions, the 6.5 at.% Mo sample has $k_{max}=0.3$ Å^{-1} and for 6.3 at.% Fe, $k_{max}=0.275$ Å^{-1}. Slightly longer length scales are thus expected in the Fe-Ge system, which can be more readily observed by comparing the CCFs.

Figs. 6b and 6c show the differential anomalous scattering results (unsmoothed and smoothed, respectively) obtained for the 6.5 at.% Mo sample. We have also obtained similar results for the 12.4 and 16.5 at.% Mo films. The relative change at the Mo edge is approximately a factor of 5-10 greater than that observed at the Ge edge. An 11% change in $f_{Mo}(E)$ causes an approximate 30% change of the main scattering peak, whereas the 16% change in $f_{Ge}(E)$ leads to a mere 6% intensity change. As with the Fe-Ge materials in the $c<0.33$ region, the Ge appears relatively homogeneously distributed whereas the Mo is inhomogeneously distributed. PSFs have not been obtained from these data. The poor Mo edge SNR introduces large uncertainties in the PSFs, if either the standard Keating[24] or Munro[23] approaches are used.

Although Mo edge data were collected for samples only at normal transmission ($\theta_k=90°$), due to the long measurement times needed to perform DAS from such weak scattering and poor detector efficiency at 20 keV, it is expected that the anomalous scattering results are similar at all oblique angles. Consistent with this view, the Ge edge data were collected for these samples at the oblique angles and little, if any, change of intensity with $f_{Ge}(E)$ is observed.

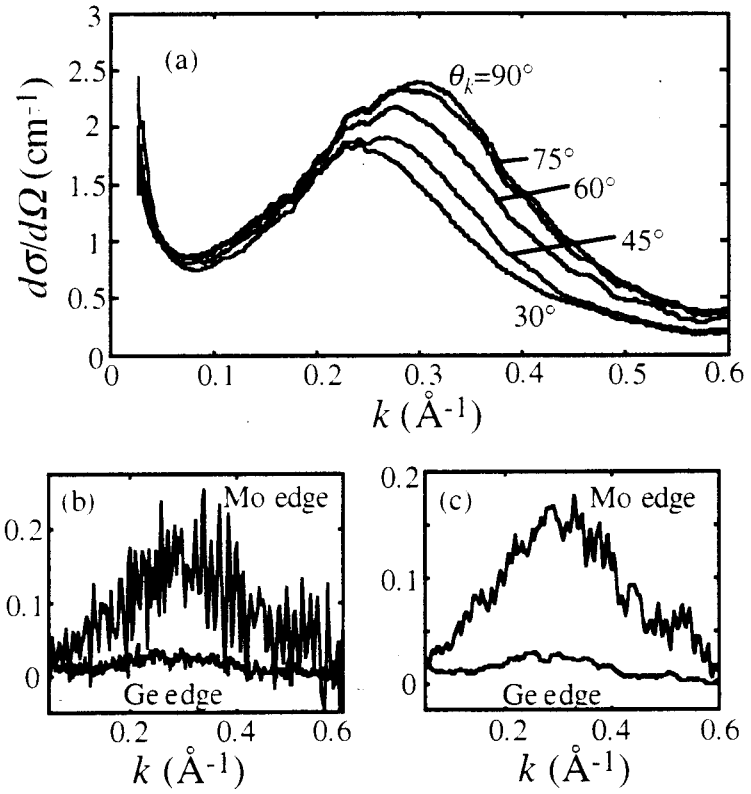

Fig. 6. (a) $d\sigma(\bar{k},E)/d\Omega$ as a function of oblique transmission angle for the 6.5 at.% Mo sample. Data smoothed over an interval Δk=0.02 Å^{-1}. (b) Absolute changes in SAXS at the Mo and Ge edges, scaled by the relative change in f′(E) at each edge (see Eq. 2). At the Ge edge, E_1=-300 and E_2=-10 eV below the edge, and E_1=-400 and E_2=-10 eV below the Mo edge. (c) Same as in (b) but smoothed over an interval Δk=0.02 Å^{-1}. Photon energy is 7100 eV.

IV. ENDPOINTS OF PHASE SEPARATION

In this section, the mean-square fluctuations in effective electron density, $\langle\eta^2(E)\rangle$, calculated from the data for several Fe-Ge and Mo-Ge samples are presented and then used to extract the endpoint compositions of the phase separation from these measurements, assuming the samples are separated into two phases. $\langle\eta^2(E)\rangle$ is readily obtained from the pair correlation function for $\bar{x}$ identically 0 (i.e. $\gamma(\bar{x}=0,E)$ in Eq. 10) and is commonly referred to as the total coherent cross-section, integrated intensity, or invariant:

$$\langle\eta^2(E)\rangle = \frac{1}{(2\pi)^3}\int S(\bar{k},E)d^3k. \qquad (4)$$

A. Mean-Square Fluctuation in Density

$\langle \eta^2(E) \rangle$ was calculated in two-dimensions with an assumed azimuthal symmetry. That is, the integral in Eq. 4 was performed by integrating each radial scan in k (for a given polar angle θ_k) and then over θ_k:

$$\frac{\langle \eta^2(E) \rangle}{n_{Ge}} = \frac{1}{n_{Ge} 2\pi^2} \int_0^{\pi/2} \left[\int_0^{\infty} S(k, \theta_k, E) k^2 dk \right] \sin\theta_k d\theta_k . \qquad (5)$$

To place the scattering in absolute units, the film thickness t must be known. Since t is not known precisely, yet the absorption edge-jump measurements at the Ge edge provide $n_{Ge}t$, with n_{Ge} the average Ge number density in the film, a factor of n_{Ge} was explicitly included in $\langle \eta^2(E) \rangle$ to properly normalize $S(\vec{k}, E)$ to sample thickness. The integral over k was performed in the usual way: the contribution from 0 to k_{min} summed with a triangular approximation, the data from k_{min} to k_{max} integrated with the trapezoidal rule, and the contribution from k_{max} to ∞ included by analytically integrating the α power law. The contribution of the triangular approximation to the total integrated intensity was usually less than 0.1%, but the contribution from the power law extrapolation can be as great as 20-30%, which is due in large part to the finite k-range sampled. The value of $\langle \eta^2(E) \rangle$ is thus largely dependent on the quality of the $1/k^{\alpha}$ extrapolation.

In these data, there was some uncertainty about which power law to choose since $4<\alpha<5$ can be quite good. Thus, the contribution to the integral was determined for two different cases (α=4 and 5), which should span the range of possible α observed. The integral over the polar angle was performed with a 7-point Simpson's rule. θ_k=0° is not experimentally accessible but is not necessary either in order to calculate $\langle \eta^2(E) \rangle$, since the $\sin\theta_k$ term in the integrand forces the θ_k=0° contribution to 0. The measurements at θ_k=90, 75, 60, 45, 30, and 15° appear sufficient to adequately sample the anisotropy.

Fig. 7 depicts the relationship between $\langle \eta^2(E) \rangle / n_{Ge}$ and $|f_{Fe}(E)|^2$ for several samples at the Fe edge and the two different power law extrapolations. There is no quantifiable change in $\langle \eta^2(E) \rangle / n_{Ge}$ with energy at the Ge edge. The different power-law extrapolations can change the overall mean-square fluctuation in density, which is due to the different assumptions that are made about the phase separation. For sharp boundaries between regions of two different electron densities, α=4, the mean-square change in electron density will be larger than that from two regions of the same difference in effective electron density but with diffuse boundaries (α=5).

- We do not have enough data to determine $\langle \eta^2(E) \rangle / n_{Ge}$ as a function of Mo edge energies since only the θ_k=90° scans were recorded at the Mo edge. At a single, lower energy (7100 eV), which allows for an improved SNR, the oblique measurements were performed on the 6.5 and 12.4 at.% Mo samples. For the 6.5 at.% Mo sample, we calculate $\langle \eta^2(E) \rangle / n_{Ge}$ to range from

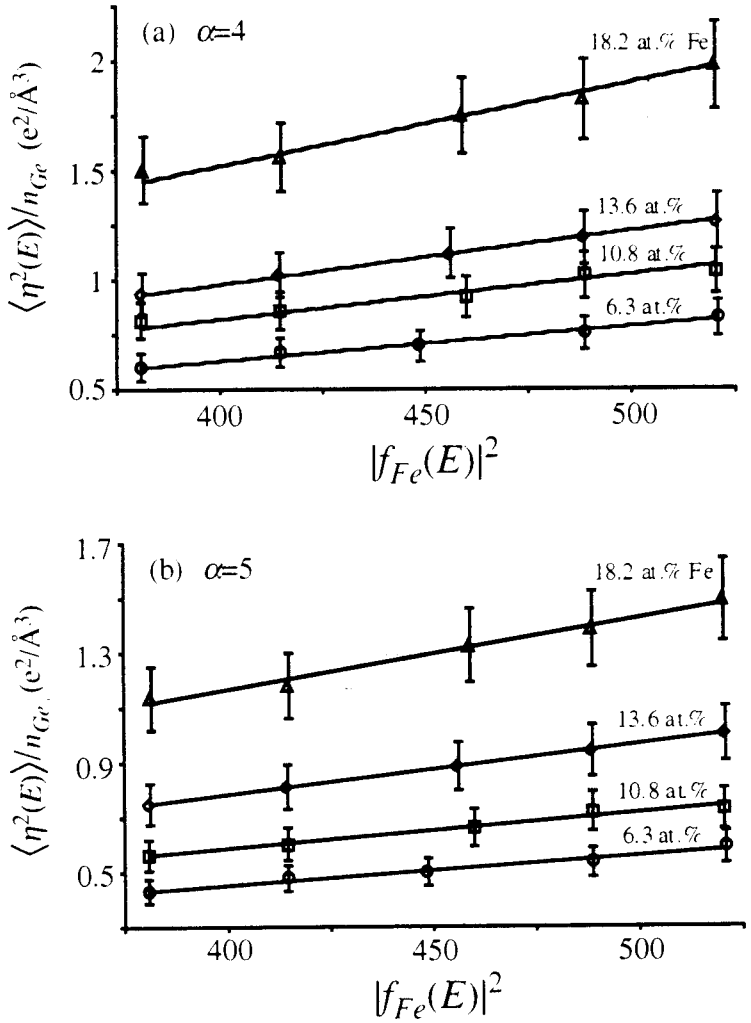

Fig. 7. Mean-square fluctuation of the effective electron density as a function of the film composition c and different power-law fall-off at large k. (a) Calculated for an α=4 fall-off (sharp transition between regions of different electron density); (b) an assumed α=5 fall-off (finite transition width).

1.54 (α=4) to 1.00 $e^2/Å^3$ (α=5), and the 12.4 at.% Mo sample, from 1.85 (α=4) to 1.19 $e^2/Å^3$ (α=5).

In what follows, two models are discussed. In the first case, it is assumed that the interfaces are sharp and the α=4 Porod law is employed to interpret the results. In the second case, a finite transition width that occupies a significant volume fraction of the sample is assumed. In either case, it is possible to determine the compositions of the phase-separating species. These two extreme examples allow us to place limits on the computed compositions, since the actual transition widths will probably vary between these two examples.

B. Model of Sharp Transition

If the samples are phase-separated into regions with sharp, abrupt interfaces, then the large k scattering obeys the Porod law. The mean-square fluctuation in effective electron density, for a two-phase system with M=Fe or Mo, is

$$\left\langle \eta^2(E) \right\rangle_{\alpha=4} = \psi(1-\psi)\left| \left(n_M^p - n_M^q\right) f_M(E) + \left(n_{Ge}^p - n_{Ge}^q\right) f_{Ge}(E) \right|^2, \quad (6)$$

with ψ the volume fraction of M_pGe_{1-p}, $(1-\psi)$ the volume fraction of M_qGe_{1-q}, and n_M^p the number density of M in M_pGe_{1-p}. The absence of a resolvable change in $\langle \eta^2(E) \rangle$ with energy at the Ge edge implies that $n_{Ge}^p = n_{Ge}^q$. In addition, it is assumed that one endpoint is amorphous Ge (i.e. p=0 or $n_M^p = 0$). Eq. 6 becomes

$$\left\langle \eta^2(E) \right\rangle_{\alpha=4} = \frac{c}{1-c} n_{Ge} \left(n_M^q - \frac{c}{1-c} n_{Ge} \right) \left| f_M(E) \right|^2, \quad (7)$$

where the volume fraction ψ is expressed in terms of the measured atomic fraction c and $n_{Ge} \equiv n_{Ge}^p = n_{Ge}^q$.

With $\langle \eta^2(E) \rangle / n_{Ge}$, $f_{Fe}(E)$, and c measured in the ASAXS and absorption experiments, a linear fit of $\langle \eta^2(E) \rangle / n_{Ge}$ to $|f_{Fe}(E)|^2$ allows one to find the slope, $\frac{c}{1-c}\left(n_{Fe}^q - \frac{c}{1-c} n_{Ge}\right)$. Then, n_{Fe}^q can be determined for a given n_{Ge} (or vice-versa), and the atomic fraction q of the phase Fe_qGe_{1-q} determined from the relationship, $q = \frac{n_{Fe}^q}{n_{Ge} + n_{Fe}^q}$. The evident linear relationship between $\langle \eta^2(E) \rangle / n_{Ge}$, calculated for α=4, and $|f_{Fe}(E)|^2$ shown in Fig. 7a, illustrates that there is good agreement with the two-phase approximation of Eq. 7. For number densities of 95% of, and the crystalline value for, crystalline Ge, the different possible endpoints q are shown in Fig. 8. The results are convincing; for all samples studied, q ranges from approximately 0.34 to 0.38 for the Fe-containing alloys.

Since the mean-square fluctuation in density is known only at one energy for the 6.5 and 12.4 at.% Mo samples, the slope method to determine the endpoint composition cannot be used. The endpoint composition can still be determined, however, by dividing out the term $|f_{Mo}(E)|^2$ in Eq. 7. Then, for a given n_{Ge}, a n_{Mo}^q can be determined and hence the composition q of phase Mo_qGe_{1-q}. This method yields endpoint compositions of approximately 24 to 27 at.% Mo for the two Mo-containing alloys that were studied.

Error bars in figs. 7 and 8 have been calculated assuming the greatest errors in our measurements are from placing the data on an absolute scale (usually no greater than ±10% with the polyethylene standard) and from determining the film composition (uncertainty of ~0.5 at.% metal). We have computed the corresponding error bars for the endpoint compositions (fig. 8),

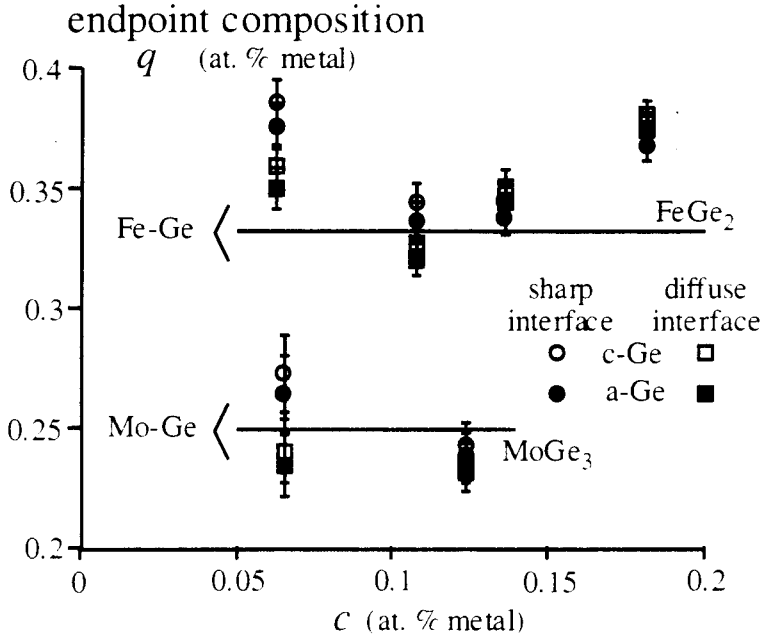

Fig. 8. Endpoint compositions q determined from the mean-square fluctuation in effective electron density for four Fe-Ge and two Mo-Ge samples, with assumed number densities of Ge that are equal to that for c-Ge and 95% of c-Ge (a-Ge). For the theory of a sharp transition between the two-phase regions, $\langle \eta^2(E) \rangle / n_{Ge}$ is determined with $\alpha=4$ and for a 50% transition width it is determined with $\alpha=5$.

using the standard deviation of the slope for the slope method (Fe-Ge alloys) or directly (Mo-Ge alloys). Clearly, the slope method provides a more refined value for the endpoint compositions.

C. Model of Diffuse Transition

Here, the other extreme is considered. It is assumed that the transition width occupies a large fraction of one of the phases. As an approximation to the electron density of the transition region, which in theory should vary continuously through the interface from one phase to the other, let the average density of the two endpoints occupy the interfacial region. With $\alpha=5$, the transition regions between the minor and major phases would consume ~40-50% of the volume of the minor phase. Then, if the volume fraction of the minor phase (which is the intermetallic for the compositions we studied) M_qGe_{1-q} is $\psi/2$ and the volume fraction of M_pGe_{1-p} (a-Ge) is $1-\psi$, the overall effective electron densities must be related by

$$\frac{\psi}{2}\rho_q + (1-\psi)\rho_p + \frac{\psi}{2}\left(\frac{\rho_q + \rho_p}{2}\right) = \rho_0, \qquad (8)$$

with ρ_q the effective electron density for M_qGe_{1-q} and ρ_0 the average effective electron density. With the same assumptions as were used in obtaining Eq. 7, the diffuse model yields

$$\left\langle \eta^2(E) \right\rangle_{\alpha=5} = \frac{c}{1-c} n_{Ge} \left(\frac{5}{6} n_M^q - \frac{c}{1-c} n_{Ge} \right) |f_M(E)|^2 . \qquad (9)$$

As in the previous example for M=Fe, the slope can be determined from Fig. 7b. This allows the determination of the atomic fraction q, given a number density for a-Ge. The different possible endpoints q are shown in Fig. 8 for two different Ge number densities. For all samples studied, q ranges from approximately 0.32 to 0.38 for the Fe-Ge samples and from approximately 0.23 to 0.24 for the Mo-Ge samples.

These two models are two extreme examples of the type of interfacial region that we suspect exist in these samples. Although we are unable to determine the interfacial structure, it appears that, regardless of the nature of the interface, the composition of the regions that are somewhat removed from the interfacial regions can be determined. In this case, it appears that there is phase separation into a-Ge and a Fe-Ge or Mo-Ge intermetallic, close in composition to an amorphous $FeGe_2$ or $MoGe_3$. This is in excellent agreement with the disappearance of the SAXS at 23.6 to 25 at.% Mo and is consistent with the structural model of Kortright and Bienenstock,[1] who argue that two different structural regions meet at approximately 23 at.% Mo. It should be noted, however, that c-$MoGe_3$ is not in the equilibrium phase diagram nor has it been observed before; alloys with this composition in the equilibrium state are phase-separated into c-Ge and c-$MoGe_2$. This, of course, does not rule out the possibility that $MoGe_3$ is a relatively stable amorphous material. For example, there is a well-defined amorphous MoS_3 even though its crystalline counterpart does not exist.[25]

V. CYLINDRICAL CORRELATION FUNCTION

In order to obtain more detailed information about the nature of the composition fluctuations, the effective electron pair correlation function,

$$\gamma(\bar{x},E) \equiv \left\langle \rho(\bar{x}+\bar{x}_0,E)\rho(\bar{x}_0,E) \right\rangle = \frac{1}{(2\pi)^3} \int S(\bar{k},E) e^{i\bar{k}\cdot\bar{x}} d^3k , \qquad (10)$$

has been calculated. Here $\rho(\bar{x},E)$ is the effective electron density at $\bar{x}$ and determined by the anomalous scattering factors and the number densities in the material. From the vapor deposition process itself, the pair correlation function is likely to exhibit an "in-plane" isotropy with an axis of cylindrical symmetry in the direction of growth. The appropriate function in this case is the cylindrically symmetric pair correlation function first discussed by Norman[13] and used for the study of oriented polymers by Milberg.[26]

In order to calculate that portion of the CCF associated with the composition fluctuations, rather than the usual radial distribution function (RDF), the integral of the RHS of Eq. 10 has been performed by extrapolating the observed SAXS intensities to infinity with the Porod law. The resulting pair correlation function contains no information about the atomic-level structure. It assumes that the electron density within a specific phase is constant and that there are sharp boundaries between regions of different electron density.

In contrast to atomic pair correlation functions (e.g. RDF) used in studies of short-range order, the "independent scattering" of the "particles" has not been removed. The observed scattering is from both intrapartiele and interparticle interference. In the RDF, it is usually desirable to remove the intraparticle scattering so that one can highlight the interparticle features. In the situation studied here, the "particles" are the phase separated regions, about which information is

sought. Thus, the CCF which is presented in this section includes the self-scattering contribution. We are presently attempting to remove the intraparticle contribution to obtain more quantitative information about the interparticle correlations.

A. Theory and Implementation of CCF

For correlation functions with cylindrical symmetry, $\gamma(\vec{x},E)$ and $S(\vec{k},E)$ can be expanded in terms of Legendre polynomials,

$$\gamma(x,\theta_x) = \sum_{n=0,2,4..}^{\infty} P_n(\cos\theta_x)\gamma_n(x) \tag{11}$$

and

$$S(k,\theta_k) = \sum_{n=0,2,4..}^{\infty} P_n(\cos\theta_k)S_n(k). \tag{12}$$

The coefficients $\gamma_n(x)$ and $S_n(k)$ satisfy the spherical Bessel transform

$$\gamma_n(x) = \frac{i^n}{2\pi^2}\int_0^{\infty} k^2 j_n(kx)S_n(k)dk, \tag{13}$$

and (x,θ_x,ϕ_x) and (k,θ_k,ϕ_k) are spherical polar coordinates in real and reciprocal space that describe $\gamma(\vec{x})$ (fig. 1). Due to the cylindrical symmetry, ϕ_x and ϕ_k do not enter into the final relations and are dropped from the notation.

The CCF, for any given film, has been calculated from data measured at one energy, so E is also dropped from the notation. Only the even terms in n are of interest, since there exists an assumed inversion symmetry with respect to the x_1-x_2 or k_1-k_2 plane. This need not be the case, however, as one can imagine a situation where correlations in the direction of film growth $+\hat{x}_3$ differ from those in the $-\hat{x}_3$ direction.[15]

The $S_n(k)$ are readily obtained from the orthogonality relations, i.e.

$$S_n(k) = (2n+1)\int_0^{\pi/2} S(k,\theta_k)P_n(\cos\theta_k)\sin\theta_k d\theta_k. \tag{14}$$

It is not possible to uniquely determine all $S_n(k)$ from the finite data collected. Instead, the anisotropic scattering data have been used to determine the first four even $S_n(k)$ from Eq. 14 by employing a 7-point Simpson's rule. For each k, there are six measured points θ_k=90, 75, 60, 45, 30, and 15°. The seventh is not measurable but not necessary to compute the $S_n(k)$, since at θ_k=0° the total integrand is 0. Fig. 9a shows the computed $S_n(k)$ for a 6.3 at.% Fe sample. The n=2 and n=4 terms are far from negligible and illustrate the importance of including the anisotropy. The n=6 term, however, is much weaker, contributing far less to the series. The $S(k,\theta_k)$

computed from the $S_n(k)$ provides an approximation of better than 2% to the raw data, except near the SAXS maximum of the θ_k=90° scan, where the greatest anisotropy is observed. Even there, the fit is no worse than 5% (Fig. 9b).

The spherical Bessel transforms of the $S_n(k)$ have been computed with a trapezoidal rule and the corresponding Legendre series summed to obtain the CCF. It should be noted that each scan in k-space has been extrapolated in the normal way in order to perform the k to x transformation. Scans are extrapolated to large k with the α=4 power law and to k=0 with a Gaussian function, $A\exp[-B(\theta_k,E)k^2]$. The extrapolation to k=0 had no discernible effect on the computed CCFs.

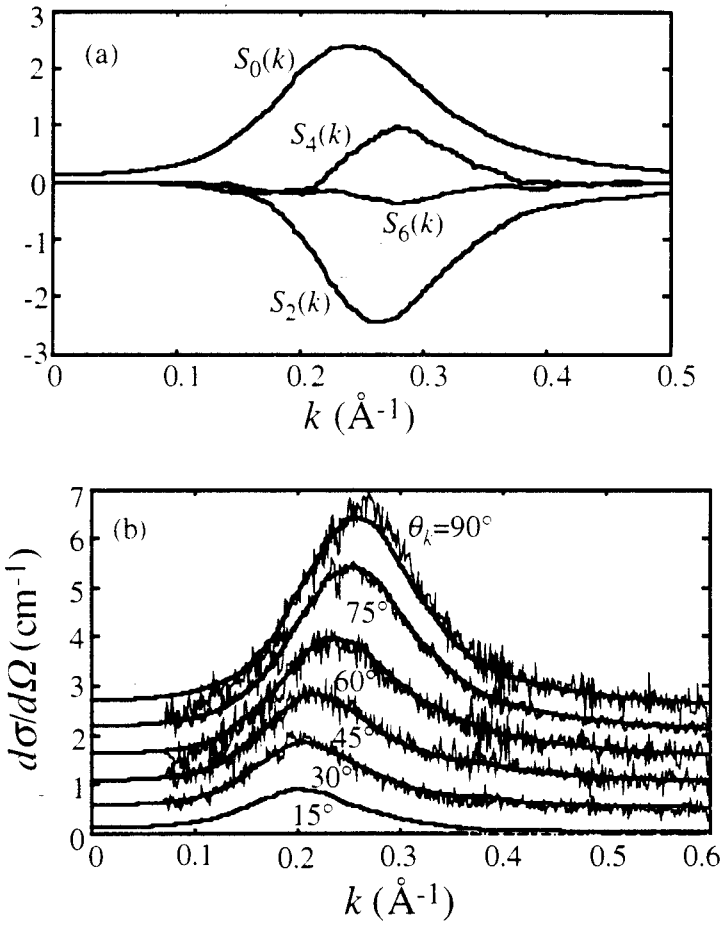

Fig. 9. (a) Legendre coefficients for the 6.3 at. % Fe sample. The n=2 and n=4 terms are far from negligible and illustrate the importance of including the anisotropy. The n=6 term, however, is much weaker, contributing far less to the series. (b) Comparison between the absolute scaled, unsmoothed data and the computed $d\sigma(\bar{k},E)/d\Omega$ from the $S_n(k)$. The Legendre sum provides an approximation of better than 2% to the data except near the SAXS maximum of the θ_k=90° scan, where the greatest anisotropy is observed and the difference from that measured is ~5%. Plots offset for clarity.

C. Results

CCFs were obtained for several of the Fe_cGe_{1-c} and Mo_cGe_{1-c} samples. In this section, the CCF of the Fe_cGe_{1-c} sample with 6.3 at.% Fe is examined in detail and then compared to the 6.5 at. % Mo sample. Comparison to, and interpretation of, the other samples' CCFs will be included in a later paper. In interpreting these CCFs, it must be remembered that they arise almost completely from fluctuations in the Fe or Mo concentrations, since the Ge is distributed essentially homogeneously.

Fig. 10 shows the computed CCF for the 6.3 at.% Fe sample with views along the radial direction x as a function of θ_x as well as a three-dimensional picture of the full CCF. The CCF has been truncated at small x in order to allow a close inspection of its cross-section in the intraparticle correlation region near $\bar{x} = 0$ and the oscillations about $\gamma(\bar{x}) = 0$. Two features are immediately apparent: (1) the intraparticle correlations extend considerably further in the growth direction than for in-plane directions, elongated by more than a factor of 50%, and (2) the radial extension in the growth direction is no greater than about 20 Å. Thus, the composition fluctuations giving rise to the SAXS cannot be well-described as columnar. If we define the average particle radii as including 90% of the maximum $\gamma(\bar{x} = 0)$, then for 6.3 at.% Fe, the basic particle radii are 12.7 Å in the growth direction by 7.3 Å in-plane. For the 6.5 at.% Mo sample shown in the figure, the corresponding dimensions are 8.8 Å by 6.3 Å.

There are oscillations in $\gamma(x,\theta_x)$ about 0 beyond the intraparticle correlations. In contrast with the RDF situation, for which the correlation function is inherently positive, the negative correlations shown here are real, resulting from deviations of the electron density from its average value, which is not included. $\gamma(x,\theta_x)<0$ indicates that the difference in electron density from the mean for two points separated by $\bar{x}$ is of opposite sign, on average. The negative $\gamma(x,\theta_x)$ just outside the intraparticle peak is often labeled a depletion region. That is, the region surrounding a $FeGe_2$ particle is deficient in Fe. This effect is most evident for the 6.3 at.% Fe sample at $\theta_x = 90^o$, the in-plane direction. As θ_x decreases to 0, corresponding to the growth direction, the depletion region is not at all evident.

At still larger x (26Å) for an in-plane direction, there is an additional maximum, corresponding to correlations in the positions of the particles. No significant maximum is observed in the growth direction. Given these particle sizes, the overall film compositions, and the recorded absolute intensities, a large packing fraction exists (also evidenced in our work with models--see Section VI). Our results indicate that little, if any, correlation between particles exists in the growth direction even though these particles are rather densely packed.

For the 6.5 at.% Mo sample, the large, positive $\gamma(x,\theta_x)$ at small x (Fig. 10c) does not extend to as large x and the anisotropy of the FWHM of the peak at small x is not as pronounced as that for the 6.3 at.% Fe sample. A well-defined depletion region exists for in-plane correlations, and there is also evidence of such a region in the growth direction. In contrast to the 6.3 at.% Fe sample, the in-plane interparticle correlations are less evident for this sample, but they are still observable. In addition, the correlations in the direction of growth appear, relative to its in-plane correlations, stronger in the Mo-containing sample than in the corresponding Fe sample.

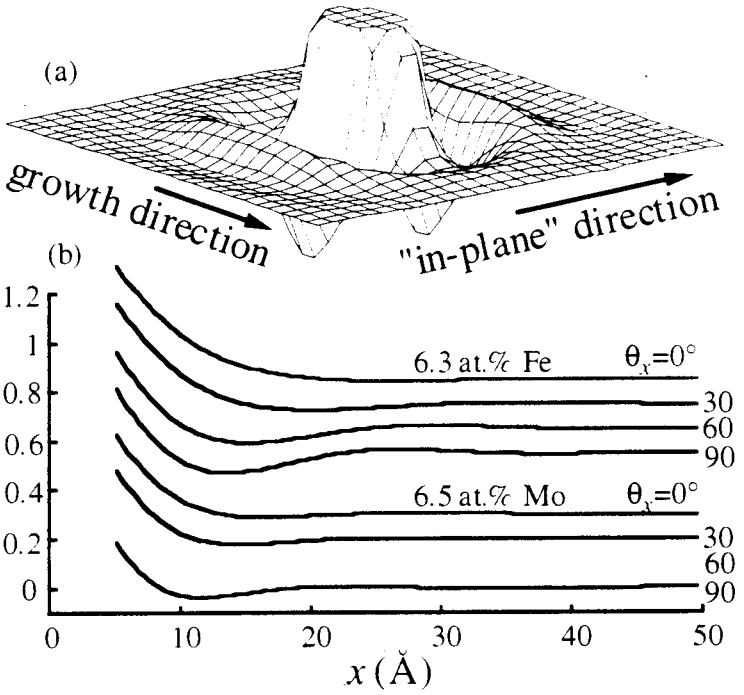

Fig. 10. CCF, $\gamma(x,\theta_x)$, in units of $(e^-/Å^3)^2$. (a) Three-dimensional mesh plot of the CCF for 6.3 at.% Fe; E=6912 eV. Mesh lines are spaced 4 Å by 4 Å. (b) 6.3 at.% Fe and 6.5 at.% Mo (E=7100 eV) CCFs along different radial directions θ_x. Plots offset and truncated at small x in order to better observe the oscillations.

VI. MODELS OF PHASE SEPARATION

In this Section, the results from the CCF are used to aid in the construction of averaged, simplified models of anisotropic phase separation. The results presented thus far indicate that the materials consist of regions of well-defined electron density, of which we have identified the metal-rich parts as $FeGe_2$ and $MoGe_3$. Thus, we consider the system as containing distinct particles embedded in a matrix, with the scattering a result of intra- and interparticle contributions Two models that we have considered reproduce the scattering results qualitatively and are discussed in detail.

A. Inhomogeneous Particles

Inhomogeneous particle models[27] have been used in the past to explain a peak at non-zero k in spherically symmetric systems, and a simple modification can be made that leads to anisotropic scattering. It is assumed that there are two regions of homogeneity in a particle of volume V_2 which is embedded in a matrix of average electron density, ρ_0. The first occupies an interior volume V_1 and has an electron density, ρ_1, while the other occupies a volume (V_2-V_1), with an electron density, ρ_2, and forms the periphery of the particle. We have taken these volumes as two confocal, prolate ellipsoids. The structure factor for such a system is given by

$$S(\vec{k},E) = \rho_p\left|(\rho_1-\rho_2)\Phi(kR_1)V_1 + (\rho_2-\rho_0)\Phi(kR_2)V_2\right|^2, \qquad (15)$$

with $R_1 = \sqrt{X_1^2\sin^2\theta_k + X_3^2\cos^2\theta_k}$ and semi-axes X_1 and X_3 for the inner ellipsoid (similarly for the ellipsoid defined by V_2), $\Phi(u) = 3\frac{\sin u - u\cos u}{u^3}$, and ρ_p the density of the particles. The composite particles are oriented with X_3 aligned in the growth direction, $\hat{x}_3$.

This equation assumes that the elongated particles are scattering independently (i.e. correlations in the positions of the particles are not taken into account). Two factors make this a reasonable assumption for this model. The first is that the CCFs (fig. 10) indicate that there is only a weak positive correlation surrounding the intraparticle peak. The most important correlation is of the higher electron density region with the low electron density region immediately surrounding it, which is automatically taken into account with this model. The second is that the particles are "constructed" so that the scattering factor of each composite particle goes to zero at small angles. As a result, the particle's scattering factor is very small in the region in which interparticle interference is appreciable. Interparticle interference effects will thus be less noticeable for this model than for one of homogeneous particles, which have a more traditional scattering factor (i.e. one that monotonically decreases as k increases).

For the compositions of the alloys that we have studied, the intermetallic phase occupies less than 50% of the total volume, and we identify volume V_1 with the intermetallic and the depletion zone (i.e. the region spanned by the difference between the inner and outer ellipsoids) with a-Ge. Since the Ge number density is constant in this model, Eq. 15 can be simplified:

$$S(\vec{k},E) = \rho_p\left|n_M^I\Phi(kR_1)V_1 - n_M^{avg}\Phi(kR_2)V_2\right|^2\left|f_M(E)\right|^2, \qquad (16)$$

with n_M^I the metal number density in the intermetallic and n_M^{avg} the average metal number density in the film. To calculate the model spectra, the volumes of the inner ellipsoid and depletion zone must be consistent with the overall film composition. For an inner region of $FeGe_2$ and depletion zone of Ge, we have $V_1/V_2 = 2c/(1-c)$. For a composition of 6.3 at.% Fe, ellipsoids of inner axes (7.5,15) Å and depletion axes (18.5,19.4) Å are in the appropriate size range and give a good reproduction of the observed anisotropy (Fig. 11a).

Since the number density of Ge is constant in this model with an inhomogeneous distribution of Fe, the model is consistent with the anomalous scattering measurements. To achieve the same magnitude of scattering as that observed, the particle density must be $\sim 3.9\cdot 10^{-5}\,\frac{\text{particles}}{\text{Å}^3}$, which fills ~100% of the sample volume with composite particles. It is important to note, however, that this only corresponds to a packing of ~14% of the inner ellipsoids (intermetallic phase). For the 13.6 at.% Fe sample, ellipsoids of (10,15) Å and (16,18.6) Å reproduce the main features of the anisotropy and amplitude change with θ_k. In this case, the particle density is $\sim 9.5\cdot 10^{-5}\,\frac{\text{particles}}{\text{Å}^3}$, which fills ~59% of the sample volume with the inner ellipsoids and 189% with composite particles. These results imply that interparticle interference must be taken into account for this sample. We have been unable, thus far, to combine the inhomogeneous particle model successfully with the interparticle interference model presented below. Work along these lines is continuing.

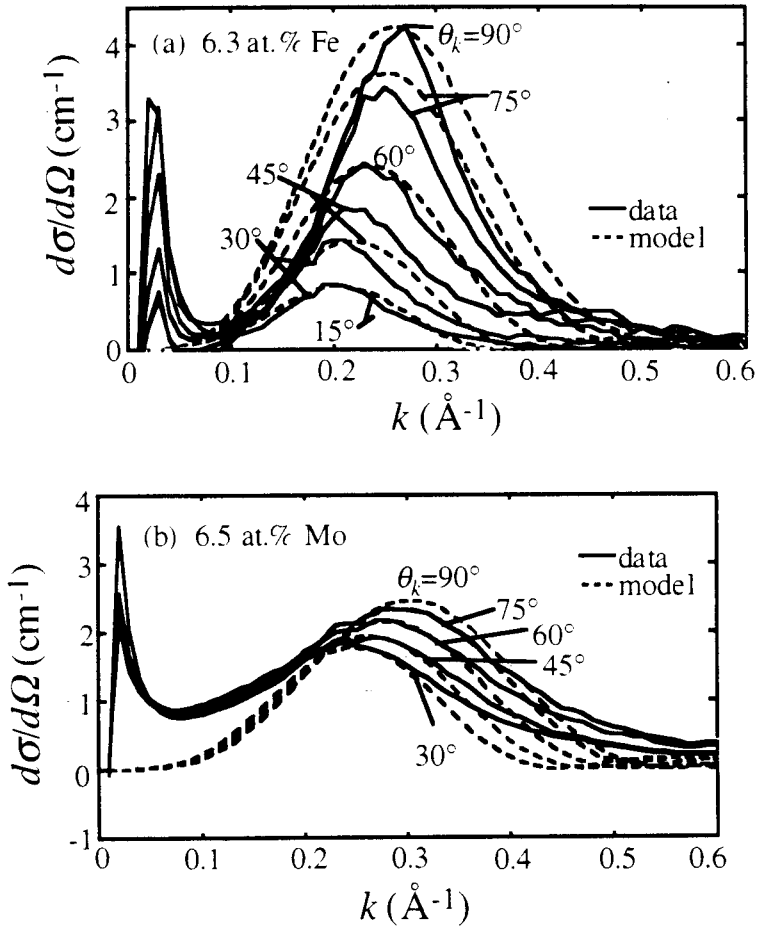

Fig. 11. Spectra from inhomogeneous particle model as compared to data from (a) the 6.3 at.% Fe [(7.5,15) Å particle and depletion region extending to (18,19.4) Å] at 6912 eV and (b) the 6.5 at.% Mo [(8,11) Å by (14,17.2) Å; 7100 eV] samples. Change in peak position and amplitude with angle agrees well with data from amorphous films. We have assumed the number density of Fe in $FeGe_2$ to be ~0.021 Å^{-3}, and Mo in $MoGe_3$ to be ~0.014 Å^{-3}. The anomalous scattering measurements can be similarly reproduced by including the appropriate changes in the atomic scattering factors with energy.

If the inner region is $MoGe_3$, then $V_1/V_2=3c/(1-c)$. Ellipsoids of (8,11) Å and (14,17.2) Å reproduce the 6.5 at.% Mo scattering patterns. The composite particles must be packed to fill 61% of the available volume to reproduce the observed scattering magnitude (Fig. 11b), or the inner ellipsoids must fill 13% of the total sample volume. Another example is one with the metal atoms located in the depletion zone, with the inner ellipsoid a-Ge. The order-of-magnitude results are similar and will not be discussed further.

With the inhomogeneous particles packed together in order to reproduce the magnitude of scattering, the depletion zones are touching if not slightly overlapping. Finally, it is important to observe that the depletion zones are more extended in the film plane than in the growth direction. To observe the appreciable anisotropy of the SAXS maximum that we report, the relative size of the depletion zone must be greater for an in-plane direction than in the growth direction.

B. Close-Packed Homogeneous Particles

The 20-30 Å spacings from the CCFs and the inhomogeneous particle model, with the outer depletion zones touching or overlapping, leads also to a model that consists of particles in an interconnected depletion zone: a close-packing of homogeneous ellipsoids in a matrix of uniform electron density. At low metal concentrations, these are particles of the Ge-rich intermetallic ($FeGe_2$ or $MoGe_3$) in a matrix of a-Ge. When the volume fraction of intermetallic phase exceeds 0.5, the particles are a-Ge, with the matrix the intermetallic phase. Again, it is assumed that all particles are identical, prolate ellipsoids with axes (X_1,X_3), and oriented such that X_3 aligns with $\hat{x}_3$. Polydispersity complicates matters but, if it is not too great, does not significantly alter the main peak positions and average particle sizes.[28] With these assumptions, the observed scattering is a product of the scattering from the individual particles and an interparticle interference function, $S_{INT}(k,\theta_k)$.

The $S_{INT}(k,\theta_k)$ used here is from the Percus-Yevick approximation[29] with a hard ellipsoid interparticle potential. With a transformation of variables, it can be shown (see Appendix) that the solution to the hard sphere Percus-Yevick equation[30] is similar to one for oriented hard ellipsoids of axes (σ_1,σ_1,σ_3). It should be stressed that the hard ellipsoid is not identical to that of the particle ellipsoid. As noted by Pederson[28] in the study of spherical precipitates in alloys, precipitates incorporate the surrounding material, and these outer regions thus define an effective hard core repulsion of somewhat larger distances than those that allow the particles to touch. In the study of inert gases or liquid metals with a true hard core repulsion, the hard core permits the closest approach between spheres to equal its diameter. In a vapor-deposited film, however, there is no real interaction between particles, particularly in the growth direction. The Percus-Yevick approach with a fictitious hard core interaction is used only to arrive at an analytic expression for the interparticle interference function.

The packing fraction, particle density, and particle and hard core ellipsoid axes are related by the overall film composition. For a model of phase separation with, for example, the $FeGe_2$ phase as the particle in a matrix of a-Ge, the packing fraction is $p_f=cV_\sigma/2V_e(1-c)$, with V_σ the hard core volume and V_e the particle volume. By choosing reasonable axes for the particle and hard core ellipsoids, the general features of the anisotropic scattering can be reproduced. The location of the SAXS maximum, change with tilt, and the order of magnitude of scattering are in agreement with the observed scattering for both the Mo and Fe based alloys.

For a 6.3 at.% Fe sample, an ellipsoid with axes (7.5,14) and (12,14) Å with a corresponding packing fraction $p_f=0.34$ works well (see Fig. 12a)--these values chosen to reproduce the peak position at each measured θ_k. There is a limit to the general features that the model can reproduce, however, especially at large packing fractions, which is the reason we have chosen not to best-fit the observed spectra to the model. The magnitude of scattering and breadth of the maximum depend critically on the shape of the Percus-Yevick interparticle function and the chosen packing fraction. The FWHM is too sharp and the magnitude of scattering is always too large to fit the data. It is expected that with a polydisperse model, the maximum would "wash out"; that is, the FWHM would increase with a corresponding decrease in the peak amplitude. The agreement between model and theory is still remarkable, however, from the order of magnitude of scattering to the reproduction of the peak position. This is a rather simple model with an ideal interparticle interference function.

The model also works well for the 13.6 at.% Fe sample, but for samples with greater Fe concentrations, the larger packing fractions lead to much sharper maxima in the interparticle function (e.g. 18.2 at.% Fe sample, intermetallic fills 45% of sample volume). In order to

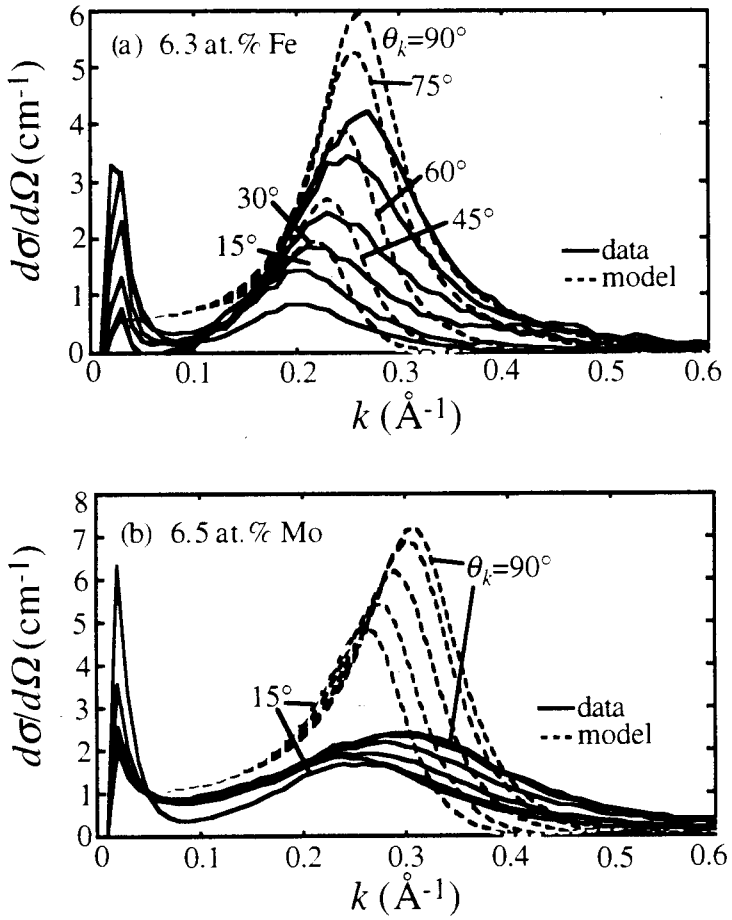

Fig. 12. Spectra from close-packed ellipsoid particle model as compared to data from (a) the 6.3 at.% Fe [(7.5,14) Å particle and hard core (12,14) Å] and (b) the 6.5 at.% Mo [(8,11) Å particle and hard core (10,12) Å] samples. Change in peak position and amplitude with angle agrees well with data from amorphous films. The number densities and photon energies are the same as in Fig. 11. The anomalous scattering measurements can be similarly reproduced by including the appropriate changes in the effective electron density with energy.

reproduce the data, the packing fraction in the Percus-Yevick model must not be too great since a large packing fraction leads to interparticle interference maxima that are quite large with narrow FWHMs. With ellipsoids of axes (12.9,18) and (13.1,18) Å and p_f=0.46, the anisotropy of the 18.2 at.% Fe sample can be reproduced. The relative change in magnitude of scattering with the change in θ_k for these ellipsoids is not good. With axes of [(13,19) by (14.5,19) Å], the relative change in magnitude of scattering is in better agreement with the data, but the larger packing fraction (p_f=0.55) leads to very sharp FWHMs that are not observed in the data. This example illustrates the main problem with the model. Whether it is from the assumption of monodispersity or the equilibrium liquid structure factor, the model leads to very sharply defined maxima (for packing fractions relevant to these materials) that are not experimentally observed.

Another interesting feature is the relative difference between the axes of the particle and hard core ellipsoids. If the particle and hard core axes are similar in the growth direction but dissimilar in the plane of the film, then the change in amplitude with tilt angle is that which is experimentally observed (decrease in magnitude as θ_k changes from 90 to 15°). Conversely, if the

particle and hard core axes are similar in the plane of the film but dissimilar in the growth direction, then the change in amplitude with tilt is exactly opposite (as θ_k changes from 90 to 15° the SAXS increases). These results indicate that, on average, the particles are not allowed to touch when they are aligned in the plane of the film ($X_1<\sigma_1$) but that they can nearly touch in the growth direction ($X_3\sim\sigma_3$).

We might consider this a quasi-columnar structure, with the possibility that the ellipsoids can touch in the growth direction but with well-defined regions of a-Ge between the ellipsoids for the in-plane directions. However, with packing fractions less than 1/2, a true columnar structure cannot be established. This result is also confirmed from the CCF and the inhomogeneous particle models, where a depletion zone is established in the film surface plane but does not appear as important in the growth direction. Although we have not shown the change in model spectra with x-ray energy, there is agreement with the anomalous scattering measurements. The M and Ge number densities in the model are such that the spectra show no change for energies near the Ge edge and a large decrease in scattering for energies that increasingly approach the M edge.

The model spectra have also been computed for a 6.5 at.% Mo sample, assuming two phases a-Ge and a-$MoGe_3$. With ellipsoids of (8,11) and (10,12) Å and p_f=0.36, the main features of the observed SAXS are reproduced (Fig. 12b). In this case, however, the computed scattering maximum is more than 2 times intense than that observed. The effects of polydispersity in the particle size and shape and in the features of the hard core are suspected to cause this effect. Even more striking, the magnitude of scattering predicted from this model of course peaks near 14 at.% Mo (where the volume fraction of the two phases, Ge and $MoGe_3$, is 1/2). However, the observed scattering does not appear to peak near 14 at.% Mo. Fig. 5 shows that the magnitude of scattering of the 6.5 and 12.4 at.% Mo samples is approximately the same.

It should be noted that we have chosen number densities for these samples based on 95% of the crystalline number densities. If the number density of $MoGe_3$ had been varied, for example, then it would have been possible to put the data and model at the same scattering magnitude. We have decided not to do this, however, since the number density of $MoGe_3$ should not deviate too greatly from a weighted average of Ge and $MoGe_2$. Finally, it is not clear whether or not the problem with fitting the 12.4 at.% Mo and 18.2 at.% Fe spectra are due to the failure of the monodisperse ellipsoid model or if the structure of the material simply cannot be modeled by ellipsoids at volume fractions near 1/2.

VII. SUMMARY AND CONCLUSIONS

In this work, normal and anomalous SAXS have been employed to characterize the composition fluctuations in sputtered amorphous Fe-Ge and Mo-Ge alloy thin films. The results indicate clearly that the "three-dimensional" characterization is consistent with the major premise of the "two-dimensional" characterization by Rice et al.[11] That is, the Ge atoms are distributed homogeneously while the metal atoms distributed inhomogeneously.

Under the assumption that there are two well-defined "phases" in the material, and that one of them is a-Ge, we find intermetallic phase separation endpoints of composition close to a-$FeGe_2$ for the Fe-Ge films and a-$MoGe_3$ for the Mo-Ge films. Although an intermetallic $MoGe_3$ does not exist in the equilibrium phase diagram, this result is consistent with the absence of a strong SAXS maximum in the 23.6 at.% Mo sample and the work of Kortright and Bienenstock[1] who argue that two different structural regions meet at a composition close to 23-25 at.% Mo.

The data appear to yield virtually the same physical model and structural interpretation no matter what method is used to analyze them. The most quantitative method is with the cylindrical correlation function (CCF). The CCFs indicate particle radii for the Fe-Ge films of the order 7-9 Å in the plane and 12-14 Å in the growth direction. For the Mo-Ge films, the corresponding dimensions are only about 5-7 and 8-9 Å, respectively.

The CCFs clearly show that there are appreciable interparticle correlations in the film plane but that they are weaker or nonexistent in the growth direction. In particular, the average particle is surrounded by a depletion region in the growth plane. Beyond the depletion region, the probability of finding a particle shows a small maximum. In the growth direction, these phenomena are much weaker or nonexistent. That is, the correlation function tends to fall off smoothly to its average value.

The data can also be simulated reasonably well with essentially equivalent homogeneous and inhomogeneous particle models involving ellipsoids which are elongated along the growth direction. In either case, the particles are either a-Ge or the relevant intermetallic, depending of which occupies less than 1/2 the volume fraction. The particle extends further in the growth direction than in-plane by a factor of approximately 1.5:1 to 2:1, with basic particle axes for a 6 at.% metal alloy approximately 13 Å in the growth direction by 7 Å in-plane for the Fe-Ge system and 11 Å growth by 8 Å in-plane for the Mo-Ge system.

The observed microstructures are, in some ways, consistent with the surface diffusion pictures first suggested by Srolovitz and Kessler[31] and with in-plane phase separation of Adams et al.[32] In these pictures, adatoms have a few seconds to rearrange on the surface before being covered by the advancing surface, where their transport is governed by the much slower bulk transport coefficients. Consequently, metal-rich regions are formed by depletion of the surrounding area via surface diffusion.

These pictures lead, however, to columnar structures, whereas the particles described here are typically only 50% larger in the growth direction than in the growth plane. The small particle sizes, coupled with the large number of particles, suggest that phase separation nucleation is easy in these materials under these growth conditions. This nucleation might result from variations in the adatom flux or appreciable-sized sputtered metal clusters.[33] As a consequence, columnar growth may be terminated by the formation of new particles as growth continues. There is little correlation between where the particles are formed in one layer and where they are formed after about 20 Å further in the growth direction.

It may be that a spinodal decomposition model is a more appropriate description of the phase separation process in these films. In that case, it would appear that a theory applicable to these systems must include fluctuations which break up the columnar coherence as well as those that initiate the separation process. To our knowledge, no quantitative models that describe the phenomena shown here have been published.

As a consequence of the unusual depletion regions, one would anticipate unique percolation properties, as discussed by Deutscher et al.[34] That is, the formation of a depletion region makes the filling of space less random than is normally assumed in percolation theories. As a consequence, percolation is likely to occur with a higher fraction of the space filled than is the case for random systems.

The unusual percolation may account for the differences often cited for the M-I and superconducting transition compositions in, for example, a-Mo-Ge. Variations in the sizes of the intermetallic and depletion regions with preparation parameters are also a likely cause of the large differences in transition compositions cited by different groups. Finally, it is probably the

presence of the intermetallic regions at compositions below the M-I transition composition that accounts for the metallic low temperature specific heat in these materials.

It should also be noted that the films studied here were grown by passing a substrate table under a Ge sputtering gun and then under either a Mo or Fe gun. Our results indicate that fluctuations in the growth direction play a pivotal role in establishing a new phase separation pattern with little correlation between where the phase separation in one layer and after 20 Å of material has been deposited. Although for each pass under the targets only 0.2 to 0.8 Å of material is deposited, one cannot help but wonder, however, if our results are related to this deposition technique. It is quite possible that different results would be obtained if two targets were pointed at the sample all the time. Similarly, the fluctuations are probably highly related to the growth parameters and deposition geometry.

The marked anisotropy that we observe on the 10-30 Å scale may also manifest itself in the short-range order (SRO) of these materials. EXAFS studies[35] of sputtered amorphous Fe-Tb, for example, show a preference for Fe-Fe and Tb-Tb pair correlations in-plane with a preference for Fe-Tb pairs in the growth direction. Such an effect may also be prevalent in the M-Ge alloys. This work also opens the possibility that there exists even greater chemical inhomogeneity in the Fe-Tb system, on the 10-30 Å scale, as we report here for Fe-Ge and Mo-Ge.

Finally, we have not addressed the question of phase separation in the Fe-Ge samples with compositions greater than 33 at.% Fe. We do not find any indication of phase separation for these samples (43.9 and 46.6 at.% Fe). This is in contrast to the observations of Lorentz et al.[5] on Fe_cGe_{1-c} for which the Fe had been triode sputtered, as well as ASAXS observations[11] on the same films, which show large SAXS signals that arise, at least partly, from phase separation. This is another indication of the sensitivity of the phase separation state to the deposition conditions. For those samples with $c<0.33$, the triode-sputtered and magnetron-sputtered samples give rise to similar SAXS spectra. This raises the question as to whether those samples show evidence of the nonmagnetic to magnetic transition (at ~40 at.% Fe) in the same way that the ones studied here do. EXAFS data which were collected during the course of this work and Mossbauer measurements currently under way[36] may help resolve this question.

ACKNOWLEDGMENTS

SSRL is funded by the DOE, Office of Basic Energy Sciences. The Biotechnology Program is supported by the NIH, Biomedical Research Technology Program, Division of Research Resources. Further support is provided by the DOE, Office of Health and Environmental Research. The authors would like to thank M.B. Fernandez van Raap, P. LeCante, M. Rice, R. Serimaa, and H. Tsuruta for useful suggestions and/or help, at various times, with the ASAXS camera. The manuscript was completed while one of us (AB) was a visiting scholar at the Laboratoire de Cristallographie, C.N.R.S, Grenoble, France, where he benefited from conversations with P. Guyot, O. Lyon and J.P. Simon.

APPENDIX

The ellipsoid model for interparticle interference in the Percus-Yevick approximation will be outlined briefly here. Since the particles are assumed identical (in orientation and size), the scattering is a product of that from each particle and from an interparticle interference function, $S_{INT}(k,\theta_k)$:

$$S(k,\theta_k) = \rho_p(\rho_1 - \rho_2)^2 V_e^2 \Phi(kR_e)^2 S_{INT}(k,\theta_k) \qquad \text{(A1)}$$

with ρ_1 and ρ_2 the electron density of particle and matrix, respectively, and V_e the particle volume. Ashcroft and Lekner[37] have shown that it is possible to find S_{INT} in closed form for a hard sphere Percus-Yevick fluid. We will show here that a transformation of variables in the Percus-Yevick equation for the oriented ellipsoids can also lead to a closed-form expression for S_{INT}.

The Percus-Yevick equation[29] for a collection of oriented, hard-core ellipsoids is the following integral equation:

$$\tau(\vec{x}) = 1 + \rho_p \int_{|\vec{x}'|<2\sigma_{\vec{x}'}} \tau(\vec{x}')d^3x' - \rho_p \int_{\substack{|\vec{x}'|<2\sigma_{\vec{x}'} \\ |\vec{x}-\vec{x}'|>2\sigma_{\vec{x}-\vec{x}'}}} \tau(\vec{x}')\tau(\vec{x}-\vec{x}')d^3\vec{x}', \text{ (A2)}$$

with $\tau(\vec{x})$ defined in terms of the pair correlation functions[38]

$$\begin{array}{ll} |\vec{x}| < 2\sigma_{\vec{x}}: & g(\vec{x}) = 0 \text{ and } c(\vec{x}) = -\tau(\vec{x}) \\ |\vec{x}| > 2\sigma_{\vec{x}}: & c(\vec{x}) = 0 \text{ and } g(\vec{x}) = \tau(\vec{x}) \end{array}, \qquad \text{(A3)}$$

and $\sigma_{\vec{x}}$ the orientation-dependent distance from the center of the hard core to a point on its surface. For a hard core, prolate ellipsoid of radii $\vec{\sigma} = (\sigma_1,\sigma_1,\sigma_3)$ oriented with σ_3 in the x_3-direction, $\sigma_{\vec{x}}$ is given by

$$\sigma_{\vec{x}}(\theta_x) = \frac{\sigma_1\sigma_3}{\sqrt{\sigma_1^2\cos^2\theta_x + \sigma_3^2\sin^2\theta_x}}, \qquad \text{(A4)}$$

with an assumed x_1-x_2 isotropy. The closest approach between two hard cores is then $2\sigma_{\vec{x}}$, which, as mentioned previously, can be greater than the distance between two particles. By transforming variables to $\vec{y} = \left(\frac{x_1}{\sigma_1},\frac{x_2}{\sigma_1},\frac{x_3}{\sigma_3}\right)$ and $\vec{y}' = \left(\frac{x_1'}{\sigma_1},\frac{x_2'}{\sigma_1},\frac{x_3'}{\sigma_3}\right)$, Eq. A2 is transformed to one for spheres of unit radii:

$$\tau(\vec{y}) = 1 + \sigma_1^2\sigma_3\rho_p \int_{|\vec{y}'|<2} \tau(\vec{y}')d^3y' - \sigma_1^2\sigma_3\rho_p \int_{\substack{|\vec{y}'|<2 \\ |\vec{y}-\vec{y}'|>2}} \tau(\vec{y}')\tau(\vec{y}-\vec{y}')d^3y', \text{ (A5)}$$

with

$$\begin{array}{ll} |\vec{y}| \le 2: & g(\vec{y}) = 0 \text{ and } c(\vec{y}) = -\tau(\vec{y}) \\ |\vec{y}| > 2: & c(\vec{y}) = 0 \text{ and } g(\vec{y}) = \tau(\vec{y}) \end{array}.$$

This is readily solved by Wertheim and Thiele's approach:[30]

$$-c(\bar{y} \le 2) = \alpha + \beta|\bar{y}| + \delta|\bar{y}|^3, \tag{A6}$$

where $\alpha = \frac{(1+2p_f)^2}{(1-p_f)^4}$, $\beta = -\frac{6p_f\left(1+p_f/2\right)^2}{(1-p_f)^4}$, $\delta = \frac{p_f}{2}\frac{(1+2p_f)^2}{(1-p_f)^4}$, and the packing fraction $p_f = V_\sigma \rho_p = \frac{4}{3}\pi\sigma_1^2\sigma_3\rho_p$. This is identical to

$$-c(\bar{x} \le 2\sigma_{\bar{x}}) = \alpha + \beta\frac{|\bar{x}|}{2\sigma_{\bar{x}}} + \delta\frac{|\bar{x}|^3}{(2\sigma_{\bar{x}})^3}, \tag{A7}$$

a form first proposed by Pynn[39] for elongated particles, but with a different p_f, that has been used in the study of the isotropic-nematic transitions in the hard ellipsoid fluid.[40]

The Fourier transform of $c(\bar{x})$, $\tilde{c}(\bar{k})$, is given by

$$-\tilde{c}(\bar{k}) = 8\sigma_1^2\sigma_3\int_{\substack{\text{unit}\\ \text{sphere}}}\left(\alpha+\beta x+\delta x^3\right)\exp\left(-i\vec{\bar{k}}\cdot\bar{x}\right)d^3x, \tag{A8}$$

where $\vec{\bar{k}} = 2\left(k_1\sigma_1, k_2\sigma_1, k_3\sigma_3\right)$. This is readily integrated in terms of elementary trigonometric functions (left to the reader) and simply related to $S_{INT}(\bar{k})$:

$$S_{INT}(k,\theta_k) = \frac{1}{1+\frac{12}{k\sigma_e}p_f\int_0^1\left(\alpha+\beta x+\delta x^3\right)\sin(2k\sigma_e x)x\,dx}, \tag{A9}$$

with $\sigma_e = \sqrt{\sigma_1^2\sin^2\theta_k + \sigma_3^2\cos^2\theta_k}$.

FOOTNOTES

* Present address: Division of Applied Sciences, Harvard University, Cambridge, Massachusetts 02138

[1]J.B. Kortright and A. Bienenstock, Phys. Rev. B **37**, 2979 (1988).
[2]S. Yoshizumi, D. Mael, T.H. Geballe and R.L. Greene, in Localization and Metal-Insulator Transitions, edited by H. Fritzsche and D. Adler (Plenum, New York, 1985), pp. 77-87.
[3]A. Devenyi, C. Rusu, A. Belu, and R. Manaila, J. De Phys. Colloque **42**, C4-1089 (1981).
[4]D. Mael, S. Yoshizumi and T.H. Geballe, Phys. Rev. B **34,** 467 (1986).
[5]R.D. Lorentz, A. Bienenstock, and T.I. Morrison, Phys. Rev B **49**, 3172 (1994).
[6]H. Daver, O. Massenet, and B. Chakraverty, Proc. Fifth Intl. Conf. Amorphous and Liquid Semiconductors, Garmish, 1973, p. 1053.
[7]K. Ding and H.C. Andersen, Phys. Rev. B **36**, 2675 (1987).
[8]A.F. Marshall and S. Yoshizumi, Mat. Res. Soc. Symp. Proc. **47**, 115 (1985).
[9]M. Audier, P. Guyot, J.P. Simon, and N. Valignat, J. Phys. Coll. **46**, C8-433 (1985).
[10]Ph. Goudeau, A. Fontaine, A. Naudon, and C.E. Williams, J. Appl. Cryst. **19**, 19 (1986). O. Lyon and J.P. Simon, Phys. Rev. B **35**, 5164 (1987).
[11]M. Rice, S. Wakatsuki and A. Bienenstock, J. Appl. Cryst. **24**, 598 (1991). M. Rice, Ph.D Thesis, Stanford University (1993).
[12]M.J. Regan, M. Rice, M.B. Fernandez van Raap, and A. Bienenstock, Phys. Rev. Lett. **73**, 1118 (1994).
[13]N. Norman, Ph.D. Thesis, University of Oslo (1954).
[14]G.S. Cargill, Phys. Rev. Lett. **28**, 1372 (1972).
[15]L.C. Wilson, Ph.D. Thesis, Stanford University (1990).
[16]P.H. Fuoss, P. Eisenberger, W.K. Warburton and A. Bienenstock, Phys. Rev. Lett. **46**, 1537 (1981).
[17]See, for example, K.F. Ludwig, Ph.D. Thesis, Stanford University (1986). J.J. Hoyt, D. DeFontaine, and W.K. Warburton, J. Appl. Cryst. **17**, 344 (1984).
[18]S. Wakatsuki, K.O. Hodgson, D. Eliezer, M. Rice, S. Hubbard, N. Gillis, S. Doniach, and U. Spann, Rev. Sci. Instrum. **63**, 1736 (1992).
[19]M.J. Regan, Ph.D. Thesis, Stanford University (1993).
[20]T.P. Russell, J.S. Lin, S. Spooner, and G.D. Wignall, J. Appl. Cryst. **21**, 629 (1988).
[21]M. Maret, J.P. Simon, B. Boucher, R. Tourbot, and O. Lyon, J. Phys. Condens. Matter **4**, 9709 (1992).
[22]P.W. Schmidt, D. Avnir, D. Levy, A. Hohr, M. Steiner, and A. Roll, J. Chem. Phys. **94**, 1474 (1991).
[23]R.G. Munro, Phys. Rev. B **25**, 5037 (1982).
[24]D.T. Keating, J. Appl. Phys. **34**, 923 (1963).
[25]J.C. Wildervanck and F. Jellinek, Z. Anorg. Allgem. Chem. **328**, 309 (1964). F.Z. Chien, S.C. Moss, K.S. Liang, and R.R. Chianelli, Phys. Rev. B **29**, 4606 (1984).
[26]M.E. Milberg, J. Appl. Phys. **34**, 722 (1962).
[27]A. Guinier and G. Fournet, *Small-Angle Scattering of X-Rays* (Wiley: New York, 1955). p. 204.
[28]J.S. Pederson, Phys. Rev. B **47**, 657 (1993).
[29]J.K. Percus and G.J. Yevick, Phys. Rev. **110**, 1 (1958).
[30]M.S. Wertheim, Phys. Rev. Lett. **10**, 321 (1963). E. Thiele, J. Chem. Phys. **39**, 474 (1963).
[31]D.J. Srolovitz and D.A. Kessler, unpublished (1989).
[32]See C.D. Adams, M. Atzmon, Y.-T. Cheng and D.J. Srolovitz, Appl. Phys. Lett. **59**, 2535 (1991), and references therein.

[33]See S.R. Coon, W.F. Calaway, M.J. Pellin, and J.M. White, Surf. Sci. **298**, 161 (1993), and references therein.
[34]G. Deutscher, M. Rappaport and Z. Ovadyahu, Solid State Commun. **28**, 593 (1978).
[35]V.G. Harris, K.D. Aylesworth, B.N. Das, W.T. Elam, and N.C. Koon, Phys. Rev. Lett. **69**, 1939 (1992).
[36]M.B. Fernandez van Raap, M.J. Regan, F.H. Sanchez, A. Bienenstock, et al., in preparation.
[37]N.W. Ashcroft and J. Lekner, Phys. Rev. **145**, 83 (1966).
[38]L.S. Ornstein and F. Zernike, Proc. Akad. Sci. (Amsterdam) **17**, 793 (1914).
[39]R. Pynn, Solid State Comm. **14**, 29 (1974).
[40]U.P. Singh and Y. Singh, Phys. Rev. A **33**, 2725 (1986). J.F. Marko, Phys. Rev. Lett. **60**, 325 (1988).